PDK-1/S6K and mTORC1 bypass systemic growth restrictions to promote regeneration

Or how can some cells proliferate, when nobody else can ?

Ananthakrishnan Vijayakumar Maya [1, 2, 3], Liyne Nogay [1, 2, 3], Lara Heckmann [1, 2, 3], Isabelle Grass [1, 2], Katrin Kierdorf [4,5] , Jörg Büscher [6], Anne-Kathrin Classen [1, 2, 5, 7] *

* Corresponding author: anne.classen@biologie.uni-freiburg.de

1 Hilde-Mangold-Haus, University of Freiburg, 79104 Freiburg, Germany
2 Faculty of Biology, University of Freiburg, 79104 Freiburg, Germany
3 International Max Planck Research School for Immunobiology, Epigenetics, and Metabolism, Freiburg, Germany
4 Institute of Neuropathology, Faculty of Medicine, University of Freiburg, Freiburg, Germany
5 CIBSS Centre for Integrative Biological Signalling Studies, University of Freiburg, Germany
6 Max Planck Institute of Immunobiology and Epigenetics, Freiburg, Germany.
7 BIOSS Centre for Biological Signalling Studies, University of Freiburg, Germany

Abstract

Tissue damage and inflammation trigger systemic signals that induce catabolic breakdown and nutrient release in distant organs, a process well-characterized in the context of tumor cachexia. While mechanisms allowing tumors to circumvent these systemic growth restrictions are known, the physiological processes that overcome inflammation-induced growth restrictions to support tissue repair and regeneration remain largely unexplored. In our study, we use a model of tissue inflammation and regeneration in developing *Drosophila* imaginal discs to dissect the key metabolic and signaling adaptations that help tissue overcome systemic growth restrictions. Our findings reveal a unique metabolic strategy used by rapidly proliferating cells in the regenerating domain. Instead of relying on the conventional Insulin-PI3K-Akt signaling pathway, these cells utilize a JAK/STAT-PDK1-S6K axis. This adaptation facilitates sustained protein synthesis and cellular growth despite the systemic catabolism associated with low insulin signaling. Specifically, we find that catabolic breakdown of the fat body is driven by the insulin-binding factor Impl2, which is expressed at the site of inflammatory damage. Notably, regenerative proliferation is also supported by mTORC1 activity and is associated with the upregulation of amino acid transporters in proliferating cells of the regenerating domain. These amino acid transporters align with a specific amino acid metabolite signature in the hemolymph, revealing a specialized metabolic program that meets the demands of fast-proliferating cells. Our work provides insight into how regenerating tissues rewire signaling pathways and adapt their metabolic growth to coordinate tissue repair with a conserved systemic nutrient provision response. These findings have important implications for understanding human diseases such as chronic wounds and cancer.

Introduction

Tissue damage and inflammation trigger a dynamic interplay between cellular signals and cell behaviors to promote repair and regeneration. Proper orchestration of these responses is crucial, as failure can lead to chronic wound healing pathologies, fibrosis, or diseases like cancer (Eming et al, 2017; Huang et al, 2022; MacCarthy-Morrogh & Martin, 2020; Pena & Martin, 2024; Rybinski et al, 2014). To better understand these diseases, a wide range of recent studies aim to dissect the pathological reprogramming of relevant metabolic circuits (Martinez-Reyes & Chandel, 2021; Stine et al, 2022; Wong & Verheyen, 2021). As cancers frequently adopt tissue repair pathways for their own advantage, these studies may also indirectly offer insights into the metabolism of tissue repair. However, a surprising gap exists in our knowledge about the precise metabolic adaptations employed by the normal physiological programs of tissue repair and regeneration (Eming et al, 2021; Eming et al, 2017; Meacham et al, 2022; Zhu & Thompson, 2019). With this study, we aim to provide insight into the local and systemic metabolic adaptations during physiological tissue repair and regeneration.

Two pathways central to metabolism and cellular growth in health and disease are the Insulin/PI3K/Akt and mTORC1 signaling pathways. Both are intimately linked by their shared effector ribosomal protein S6 kinase (S6K), which drives protein synthesis and cellular growth by activating protein translation. Insulin/PI3K/Akt is activated by binding of Insulin to its receptor (InR), thereby stimulating Phosphoinositide-3-kinase (PI3K) to produce Phosphatidylinositol (3,4,5)-trisphosphate (PIP3) at the plasma membrane. PIP3 recruits Phosphoinositide-dependent kinase 1 (PDK-1), but also activates Akt, which inhibits nuclear translocation of the transcription factor dFOXO and promotes survival. PDK-1 in turn phosphorylates and activates S6K, yet, for S6K to function optimally, at least two of its residues need to be phosphorylated. In addition to PDK-1, the mechanistic target of rapamycin complex 1 (mTORC1) and c-Jun N-terminal kinases (JNK) phosphorylate activating residues on S6K (Holz et al, 2005; Hopkins et al, 2020; Hoxhaj & Manning, 2020; Manning & Cantley, 2007; Wu et al, 2022). mTORC1 is central to anabolic growth by modulating cellular responses to nutrient availability and environmental cues (Saxton & Sabatini, 2017). While it is sensitive to amino acid availability, it can also be stimulated by Akt via crosstalk with Insulin/PI3K/Akt signaling. The interplay of Insulin/PI3K/Akt and mTORC1 signaling in metabolism is highly conserved from invertebrates to vertebrates. Previous studies demonstrated that Insulin signaling is active in *Drosophila* epidermal wounds, where it facilitates epithelial sealing by regulating actin dynamics immediately after damage (Kakanj et al, 2016; Nakamura et al, 2020). Recent evidence reveals an elevation of ribosomal S6K phosphorylation in mammalian skin wounds and correlating it with successful healing (Ring et al, 2023). Yet, the relevant molecular mechanisms and precise metabolic adaptations during repair responses have yet to be investigated.

Drosophila models have significantly advanced our understanding of tissue repair, regeneration and metabolism (Fox et al, 2020; Worley & Hariharan, 2022). Specifically, studies in developing wing imaginal

discs or the adult gut have highlighted the role of two key signaling pathways - JNK/AP1 and JAK/STAT signaling - in epithelial repair and proliferation. The JNK/AP1 pathway is an early stress response pathway which induces a senescence-like cell cycle arrest the site of tissue damage (Cosolo et al, 2019; Floc'hlay et al, 2023; Jaiswal et al, 2023). The senescence-like state is associated with the production of extracellular matrix and cytoskeletal remodelers, which promote the sealing of epithelial wounds (Floc'hlay et al, 2023; Nakamura et al, 2020; Pena & Martin, 2024; Stevens & Page-McCaw, 2012). Importantly, these cells also produce Unpaired (Upd) cytokines. Their paracrine activity activates JAK/STAT in cells surrounding the site of inflammatory damage, where it promotes cell survival and compensatory proliferation during tissue regeneration (Crucianelli et al, 2022; Floc'hlay et al, 2023; Herrera & Bach, 2019; Jaiswal et al, 2023; La Fortezza et al, 2016; Santabarbara-Ruiz et al, 2015; Worley et al, 2022). Compensatory proliferation itself is characterized by an accelerated cell cycle with shortened S-phases and gap phases (**Fig S1A**) (Crucianelli et al, 2022; Herrera et al, 2013; Sustar et al, 2011). The distinct functional and proliferative demands of senescent and fast-proliferating cell populations within the damaged tissue raises questions about how these distinct cell populations metabolically adapt to successfully support tissue repair.

Tissue repair and tumor development share striking similarities; in fact, tumors have long been compared to non-healing wounds (Dvorak, 1986). Accordingly, *Drosophila* tumor models activate JNK/AP1 and JAK/STAT signaling, which promotes tumor progression (Enomoto & Igaki, 2022; Herrera & Bach, 2019; La Marca & Richardson, 2020). To support their growth, tumors secrete signaling molecules that initiate inter-organ signaling and systemic metabolic responses (Bilder et al, 2021; Hodgson et al, 2021; Liu et al, 2022). For instance, the Insulin-like peptide 8 (Dilp8), when secreted by tumors, disrupts hormone balance by reducing Ecdysone and Insulin production through direct effects on the ring gland and Insulin-producing cells (IPCs), with the effect of halting developmental progression of the tumor-bearing host (Colombani et al, 2012; Garelli et al, 2012). Other cytokines, such as Upd2, Upd3, PDGF- and VEGF-related factor 1 (Pvf1), Ecdysone-inducible gene L2 (Impl2), matrix metalloprotease 1 (MMP-1) or the TNFα homologue Eiger (Egr), directly or indirectly trigger catabolic lipolysis and proteolysis to promote nutrient release from muscles and the so-called fat body, an adipose tissue central for nutrient storage and energy homeostasis (Agrawal et al, 2016; Ding et al, 2021; Figueroa-Clarevega & Bilder, 2015; Hodgson et al, 2021; Lodge et al, 2021; Rajan & Perrimon, 2012; Romao et al, 2021; Song et al, 2019). Amino acids or sugars are released in this manner and subsequently absorbed by tumors and facilitate their anabolic growth (Cong et al, 2021; Khezri et al, 2021; Newton et al, 2020). This inter-organ signaling network and metabolic state resembles cachexia, a clinical syndrome characterized by weight loss, muscle atrophy and fatigue, typically observed in chronic inflammatory conditions, including cancer (Argiles et al, 2014; Bilder et al, 2021; Hodgson et al, 2021; Liu et al, 2022; Setiawan et al, 2023). However, the systemic and metabolic regulation of non-pathological tissue repair and regeneration remains poorly understood. Previous studies suggest that cytokines may also be released upon physiological tissue damage or starvation (Colombani et al, 2012; Garelli et al, 2012; Gontijo & Garelli, 2018; Hackney &

Cherbas, 2014; Halme et al, 2010; Sun & Poss, 2023). Further studies demonstrated the activation of fat body catabolic pathways with effects on Methionine, S-adenosylmethionine and Kynurenine metabolism promote effective imaginal disc regeneration (Kashio & Miura, 2020; Kashio et al, 2016). While these studies affirm that tumors may hijack tissue repair mechanisms, the underlying local and systemic metabolic adaptations that evolution developed to promote physiological processes of repair and regeneration remain little characterized. In our study we combine genetic analysis, quantitative imaging, untargeted metabolomics and information from single-cell RNA sequencing data to outline the local and systemic adaptations that selectively support fast-proliferating cells during regeneration through an Insulin-independent JAK/STAT-PDK1-S6K signaling axis.

Results

(1) The proliferating domain maintains high levels of protein synthesis during regeneration

Does tissue damage alter metabolic processes to drive regenerative proliferation within epithelial cells? To induce inflammation and regeneration, we expressed the *Drosophila* homologue of TNF-α, known as Eiger (Egr), for a 24 h period within the imaginal wing pouch using the *rn-GAL4* driver (Cosolo et al, 2019; Smith-Bolton et al, 2009). As previously observed, this led to significant cell death, accompanied by the activation of the JNK/AP-1 activity reporter TRE-RFP (**Fig 1A-C; Fig S1B,C**) (Chatterjee & Bohmann, 2012; Cosolo et al, 2019; Jaiswal et al, 2023; La Fortezza et al, 2016). JNK activation at the center of the pouch pauses the cell cycle in G2, as evidenced by FUCCI cell cycle analysis and the absence of EdU incorporation (**Fig 1A,B; Fig S1D-F**) (Cosolo et al, 2019; Floc'hlay et al, 2023; Jaiswal et al, 2023; Zielke et al, 2014). The JNK signaling domain exhibits characteristic features of cellular senescence, including the expression of senescence-associated-β-galactosidase (SA-β-gal) (**Fig S1G,H**), the matrix metalloprotease MMP-1 and mitogenic cytokines of the Upd family (Floc'hlay et al, 2023; Jaiswal et al, 2023). They induce compensatory proliferation in surrounding cells, which can be detected by rapid EdU incorporation (**Fig 1A,B**) (Crucianelli et al, 2022). We found that the majority of cells undergoing proliferation were located within 40 µm from the outer border of high JNK signaling cells (**Fig 1D**). To facilitate quantification of cell behaviors by TRE-RFP segmentation (see Materials and Methods) and account for disc size variation among the many experiments carried out in this study, we define a conservative 20µm band outside the high JNK signaling domain as the 'proliferative domain' (PD^{egr}) for the remainder of this study.

How can these rapidly proliferating cells be supported by biosynthesis and cellular growth? To answer this question, we monitored protein translation using O-propargyl-puromycin (OPP)-incorporation assays (Aviner, 2020). This assay revealed uniform protein synthesis levels throughout control wing imaginal discs. In the regenerating domain of *egr*-expressing discs protein translation proceeded at levels similar to control discs and was mildly reduced within the domain of high JNK-signaling, senescent cells (**Fig 1E-G**). Surprisingly, OPP incorporation significantly decreased in the notum of *egr*-expressing discs and

aligned with markedly low levels of EdU incorporation in these domains (**Fig 1H-M**). This observation suggests that protein synthesis rates as well as cell cycle entry and progression slow down significantly in cell populations at a distance from the site of tissue damage.

To test whether reduced proliferation in the notum of *egr*-expressing discs is connected to a senescent cell cycle arrest, we closely monitored JNK/AP-1 activation (TRE-RFP), cell cycle dynamics (FUCCI) and the senescence marker SA-β-GAL in the notum. However, we observed no elevation of JNK signaling nor SA-β-GAL activity, and FUCCI profiles were similar in control and *egr*-expressing disc (**Fig 1H,I; Fig S1G-J**). This suggests that the reduced proliferation in nota is distinct from JNK/AP-1-associated senescence responses in *egr*-expressing cells of the pouch. Hence, we conclude that the notum state may be more accurately described by the term quiescence.

Combining these observations, at least three distinct cell populations exist in the wing discs with inflammatory lesion, each characterized by different proliferative potentials and cellular programs: 1) a senescent cell population at the center of damage, exhibiting high protein synthesis, high JNK/AP-1 activation and a G2 cell cycle arrest; 2) an actively cycling cell population exhibiting high protein synthesis and low JNK/AP-1 activation; 3) a distal quiescent cell population displaying low rates of protein synthesis, low JNK/AP-1 activation and slow cycling activity (**Fig 1N,O**).

(2) Peripheral organs reduce growth

The lack of damage-associated signals in the notum may suggest that not local, but paracrine and even systemic changes reduce cell proliferation and biosynthesis. To investigate this, we first evaluated mitotic activity and protein synthesis in other peripheral tissues, such as the eye and leg imaginal disc. In larvae carrying *egr*-expressing wing discs, the mitotic wave anterior to the morphogenetic furrow in the developing eye was arrested, which also correlated with reduced protein synthesis (**Fig 2A-F**). Similarly, protein synthesis was diminished in leg discs, if compared to leg discs of wild type larvae (**Fig S2A,B**). Taken together, these findings reveal a widespread decline in cell proliferation and protein synthesis in *egr*-expressing larvae including distant tissues. These observations are consistent with previous reports on reduced eye disc and notum sizes after activation of stress responses in the wing pouch (Boulan et al, 2019).

We previously reported that *egr*-expressing larvae also exhibit a significant delay in initiating pupariation (La Fortezza et al, 2016). Accordingly, JNK activation in *egr*-expressing wing discs correlates with a pronounced increase in Dilp-8 expression likely underlying the delay in pupariation (**Fig 2G,H**) (Floc'hlay et al, 2023). Yet, previous studies also suggest, that Dilp8 and Egr itself may inhibit IPCs in the brain, indicating that *egr*-expressing larvae may experience low systemic Insulin signaling, limiting anabolic growth despite nutrient intake by feeding (Agrawal et al, 2016; Figueroa-Clarevega & Bilder, 2015; Ingaramo et al, 2020; Rajan & Perrimon, 2012; Vallejo et al, 2015). To understand if reduced protein

198 synthesis in distant tissues of *egr*-expressing larvae may indeed correspond to reduced systemic Insulin
199 signaling, we examined expression levels and nuclear localization of the dFOXO transcription factor, a
200 key mediator of Insulin signaling. Indeed, we observed elevated nuclear levels of FOXO in the peripheral
201 organs of the fat body dissected from *egr*-expressing larvae, if compared to wild-type controls (**Fig 2I-K**).
202 Combined, these observations strongly indicate that attenuation of Insulin signaling may occur within
203 distant non-inflamed tissues within 24 h of *egr*-expression, similar to systemic changes induced by
204 inflammatory tumors or related types of tissue damage (Ding et al, 2021; Figueroa-Clarevega & Bilder,
205 2015; Garelli et al, 2012; Hodgson et al, 2021; Jiang et al, 2022; Khezri et al, 2021; Lodge et al, 2021; Song
206 et al, 2019) .
207
208 **(3) Amino acid importers, mTORC1 signaling and ribosomal S6 phosphorylation support**
209 **regenerative proliferation**
210 How can the proliferative domain maintain protein translation, anabolic growth and proliferation a
211 systemic environment characterized by reduced protein synthesis and proliferation? To answer this
212 question, we analyzed regulatory inputs into protein translation and ribosome activity. We found that
213 transcript levels of S6K were upregulated in the wound-associated clusters of *egr*-expressing wing
214 imaginal discs in previously published scRNA-seq data sets (**Fig S3A,B**) (Floc'hlay et al, 2023), suggesting
215 that *S6K* may be regulated by the tissue repair program. Importantly, staining for phosphorylated
216 ribosomal S6 (p-S6) indeed revealed that the proliferating domain of *egr*-expressing discs exhibited
217 strongly elevated p-S6 levels (**Fig 3A-C**). This finding is in line with recent observations during wound
218 healing in mammalian skin (Ring et al, 2023). This suggests existence of a conserved mechanism that
219 elevates ribosomes activation in proliferating cells of the regenerating domain to specifically support their
220 growth.
221
222 S6K is activated by Insulin/PI3K/Akt and mTORC1 signaling (**Fig S3C**) (Liu & Sabatini, 2020; Wu et al, 2022).
223 Therefore, we assessed the activity of these two pathways in *egr*-expressing discs. To demonstrate that
224 the mTORC1 pathway is required to drive protein synthesis during wing disc regeneration, we inhibited
225 mTORC1 activity by feeding *egr*-expressing larvae the mTOR inhibitor Rapamycin for 24 h during *egr*-
226 expression (Li et al, 2014; Wu et al, 2022). Protein synthesis in control imaginal discs was only mildly
227 reduced by Rapamycin treatment. However, a pronounced reduction in protein synthesis could be
228 observed in the proliferating domain of *egr*-expressing discs upon Rapamycin treatment, demonstrating
229 that mTORC1 activity is specifically required to drive protein synthesis in the proliferating domain of *egr*-
230 expressing discs (**Fig 3D-H**).
231
232 mTORC1 activity itself is induced by uptake of nutrients and different amino acids (Jewell et al, 2013;
233 Lama-Sherpa et al, 2023; Liu & Sabatini, 2020; Shimobayashi & Hall, 2016; Yue et al, 2022). We thus
234 investigated if amino acids could be taken up preferentially by the proliferating cells in *egr*-expressing
235 discs. Indeed, transcripts of solute carrier group of membrane transport proteins (SLC) were upregulated

in *egr*-expressing discs, such as *CG15279*, a putative glycine and proline transporter of the SLC6 family, *path*, a putative alanine and glycine transporter of the SLC 36 family, *mnd*, an amino acid/polyamine transporter involved in leucine import and *CG5535*, a putative lysine, arginine, and ornithine transporter of the SLC7 family (**Fig S3D**). Importantly, we could verify upregulation of CG5535 in the proliferating domain by immunofluorescence (**Fig 3I-K**) and were similarly able to detect upregulation of CG1139 (Arcus), a putative alanine, glycine and proline transporter of the SLC36 family in *egr*-expressing discs (**Fig S3E,F**). These observations suggest that amino acids could be preferentially imported by proliferating cells. Furthermore, CG3168, a potential sugar transporter of the SLC 22 family and TRET-1, predicted to transport the disaccharide trehalose into cells (**Fig S3G-I, Fig S3D**), were strongly upregulated, indicating that additional energy sources can be imported preferentially by proliferating cells. Availability of energy would promote mTORC1 activity, as ATP production serves as a positive regulator of mTORC1 activity by inhibiting the mTORC1 antagonist AMPK (Jewell et al, 2013; Liu & Sabatini, 2020; Shimobayashi & Hall, 2016).

If the regeneration domain displays elevation of specific amino acid transporters, then what kind of changes to amino acid composition can be observed in the hemolymph of *egr*-expressing larvae which could be taken up by proliferating cells? We performed an untargeted metabolomic analysis of the hemolymph from both control and *egr*-expressing larvae. Our results revealed an enrichment of many amino acids in *egr*-expressing larval hemolymph, including those which have been reported to directly or indirectly activate mTORC1 signaling (for example, Leucine, Arginine, Glutamine (Lama-Sherpa et al, 2023; Yue et al, 2022)). Surprisingly, many come enriched in form of mixed dipeptide species. Moreover, elevated levels of dipeptide species and free amino acids associated with glutamate metabolism were observed, including increased concentrations of glutamine, glutamate, and glutamyl dipeptides (**Fig 3L**). These findings suggest that metabolic processes centered around glutamate conversion and glutaminolysis may support regenerative metabolism (Altman et al, 2016). Notably, we also observed a strong signature of urea cycle and arginine metabolism, characterized by high levels of ornithine, N-acetyl-arginine, aspartate, but low levels of argininosuccinic acid, citrulline, and N-acetyl-ornithine. This metabolite pattern together with the elevated expression of the ornithine transporter CG5535 in *egr*-expressing discs could support an increased flux of the urea cycle from ornithine towards arginine to provide a nitrogen acceptor for glutaminolysis, and potentially function to produce arginine, polyamines, nitric oxide or non-essential amino acids (Keshet et al, 2018; Lieu et al, 2020; Marti & Reith, 2021). This altered metabolite composition in the hemolymph of *egr*-expressing larvae may represent a highly flexible supply of building blocks not only for protein synthesis, but also for energy and co-factor production or glutathione redox metabolism. Combined, our data support a potential role for mTORC1 activation, amino acid uptake and glutamate and arginine metabolism in supporting the rapid growth and proliferation of the regenerating domain.

(4) Impl2 from wing discs induces a catabolic phenotype in the larval fat body

So how may these amino acids get enriched in the hemolymph of *egr*-expressing larvae? Previous studies have shown that cytokines can induce the catabolic conversion and release of nutrients from distant organs. Specifically, the break-down of fat body, muscle degradation and autophagy of imaginal discs have been established as nutrient sources driving tumor growth (Ding et al, 2021; Figueroa-Clarevega & Bilder, 2015; Katheder & Rusten, 2017; Khezri et al, 2021; Lodge et al, 2021; Newton et al, 2020; Song et al, 2019). We wanted to better understand if similar catabolic changes may be induced by *egr*-expressing larvae to facilitate regeneration. To this end, we employed Nile Red staining to visualize lipid droplets within the fat body, performed F-actin staining to observe the morphology of body wall muscles, and visualized the autophagy marker Ref(2)P in peripheral imaginal disc tissue. We did not observe changes to muscle morphology nor imaginal disc autophagy in *egr*-expressing larvae, suggesting that these tissues may not serve as a primary source for nutrients during early stages of tissue repair (**Fig S4A-D**). However, in the fat body, we observed morphological changes consistent with nutrient mobilization, such as increased droplet size and roundness, indicating that the observed hemolymph changes may be derived from fat body catabolism (**Fig 4A-D**)

In addition to the cachexic cytokines Egr and Pvf1 (Agrawal et al, 2016; Song et al, 2019), expression of all Upd family members, including Upd3, and the Insulin-growth factor binding protein Impl2, was strongly elevated in *egr*-expressing discs (**Fig 4E-J, Fig S4E**). Impl2 has been previously described as contributing to fat body break-down in adult flies with Ras^{V12}, *scrib* or Yki-dependent tumors (Ding et al, 2021; Figueroa-Clarevega & Bilder, 2015; Kwon et al, 2015), while Upd3 induces JAK/STAT signaling and acts on fat bodies during tumor growth in larval and adult hosts (Ding et al, 2021; Romao et al, 2021). Indeed, we observed activation of the JAK/STAT reporter 10xSTAT-GFP in the fat body of *egr*-expressing larvae, suggesting that *egr*-expressing discs may affect fat body signaling as well (**Fig 4K-M**). Moreover, when we ectopically expressed Impl2 for 24 h using the wing-specific driver rn-GAL4, we found that this was sufficient to induce morphological changes in the fat body characteristic of nutrient mobilization (**Fig 4N-Q**). These observations indicate that the production of Impl2 and Upd cytokines from *egr*-expressing discs are likely responsible to drive nutrient mobilization from the fat body, thereby enriching the hemolymph with metabolites that support regenerative proliferation.

(5) PDK-1 acts independent of Insulin/PI3K/Akt signaling in S6K activation and is regulated by JAK/STAT signaling

Nutrient availability, along with mTORC1 activation, are not sufficient to elevate levels of protein synthesis in the proliferating domain. S6K requires activation by mTORC1, but also by the kinase PDK-1, the latter being integral to Insulin/PI3K signaling (Hopkins et al, 2020; Hoxhaj & Manning, 2020; Wu et al, 2022). If *egr*-expressing discs induce low systemic Insulin signaling, could the proliferating domain somehow activate Insulin/PI3K signaling to drive PDK-1 activity towards S6K?

311 To understand if Insulin/PI3K and downstream signaling effectors are active in proliferating cells, we
312 examined the nuclear localization of dFOXO, the downstream effector of Insulin/PI3K/Akt activity in the
313 proliferating domain. Strikingly, we observed that both cytoplasmic and nuclear levels of dFOXO were
314 elevated, suggesting that both dFOXO levels, as well as rates of nuclear translocation were upregulated
315 (**Fig 5A-C**). The high nuclear dFOXO levels in the proliferating domain strongly suggests that also locally,
316 Insulin/PI3K signaling is low in proliferating cells. This is consistent with a systemic environment of low
317 Insulin signaling. Our conclusion is further supported by experiments showing that InR levels remained
318 unchanged, and levels of Akt and phosphorylated Akt (P-Akt) were even reduced in the regenerating
319 domain (**Fig S5A-H**). Consequently, the proliferating domain has not evolved an Insulin-scavenging
320 mechanism to maintain high levels of protein synthesis in a growth restrictive environment with low
321 Insulin signaling.
322
323 Given this observation, the question arises as to how else S6K may become co-activated by PDK-1.
324 Strikingly, we observed that the expression of PDK-1 was strongly upregulated in the proliferating domain
325 (**Fig 5D-F**). Elevated PDK-1 protein levels may arise from post-translational mechanisms affecting PDK-1
326 stability, as we did not observe an increase in PDK-1 transcripts (Floc'hlay et al, 2023). We wanted to
327 identify the upstream regulator of PDK-1 elevation. In *egr*-expressing discs, JAK/STAT signaling is
328 activated in the proliferating domain to promote cell proliferation and survival (**Fig S5I,J**) (Crucianelli et
329 al, 2022; Jaiswal et al, 2023; La Fortezza et al, 2016). To test whether JAK/STAT signaling may regulate
330 PDK-1 levels, we expressed STAT92E using the *en-GAL4* driver in the posterior compartment of wing
331 imaginal discs, which drives JAK/STAT activation (Jaiswal et al, 2023). We found that JAK/STAT activation
332 increased the levels of PDK-1-GFP, phospho-S6 and protein synthesis (**Fig 5G-O**). This suggests that
333 JAK/STAT activation in the proliferating domain increases PDK-1 levels and thereby promotes ribosomal
334 S6 phosphorylation and protein synthesis. Combined, these observations reveal a novel function for
335 JAK/STAT in tissue repair and regeneration and outline a pathway whereby the combined action of PDK-1
336 and mTORC1 drives insulin-independent growth within the proliferating domain.
337
338 **(6) PDK-1 is necessary and sufficient to drive Insulin-independent regenerative proliferation**
339 To provide evidence that upregulation of PDK-1 levels plays a crucial role in the proliferating domain of
340 *egr*-expressing discs, we tested whether ectopic expression of PDK-1 alone was sufficient to drive protein
341 synthesis and promote growth of wing disc tissues. We therefore expressed either a wild-type form of
342 PDK-1 or a constitutively active form of PDK-1 for 24 hours in the wing pouch using the *rn-GAL4* driver.
343 Compared to control discs, we observed higher levels of protein synthesis and larger pouch sizes in both
344 PDK-1-expressing genotypes. The increased size of the pouch appeared to be supported by cell
345 proliferation, as EdU incorporation in PDK-1 expressing domains was clearly elevated (**Fig 6A-F, Fig S6A-**
346 **D**). These results align with previous studies (Radimerski et al, 2002; Rintelen et al, 2001) and
347 demonstrate that high PDK-1 levels are sufficient to support a metabolic program characteristic of
348 regenerative proliferation. Importantly, PDK-1 can auto-activate via transphosphorylation upon PIP3-

349 dependent recruitment to the plasma membrane (Levina et al, 2022). We therefore analyzed PIP3 levels
350 using the pleckstrin-homology domain reporter tGPH in *egr*-expressing discs (Britton et al, 2002). tGPH
351 levels at the membrane were consistently high, suggesting that PIP3 levels are not reduced in *egr*-
352 expressing discs and that the plasma membrane provides a functional substrate for PDK-1 recruitment
353 and autoactivation (**Fig S6E,F**).
354
355 To provide proof that PDK-1 function is also necessary to support the proliferative domain in *egr*-
356 expressing discs, we genetically reduced PDK-1 function by establishing heterozygosity for a null allele of
357 PDK-1 (Rintelen et al, 2001). Importantly, heterozygous control discs did not exhibit difference in protein
358 synthesis if compared to wild type discs, revealing that heterozygosity for PDK-1 does not limit the growth
359 during normal development. However, protein synthesis in the regenerating domain of *egr*-expressing
360 discs heterozygous for PDK-1 was significantly reduced (**Fig 6G-K**). These experiments demonstrate that
361 specifically the proliferating domain is sensitive to a reduction in PDK-1 levels, and that elevated PDK-1
362 levels are necessary for protein synthesis during regenerative proliferation. Notably, the fact that
363 overexpression of a wild-type PDK-1 alone is sufficient to promote proliferation and protein synthesis,
364 suggests that PDK-1 activity can be regulated via its protein levels alone, and as such potentially
365 independent of other canonical upstream signaling inputs, such as Insulin/PI3K signaling. Strikingly, PDK-
366 1 may also be a target of systemic regulation during growth restriction, as we found that PDK-1 levels were
367 lower in peripheral tissues of *egr*-expressing larvae, such as in the eye discs (**Fig 6L-N**). This indicates that
368 PDK-1 downregulation in peripheral tissues may be an effector of the systemic changes to reduce protein
369 synthesis and anabolic growth, further positioning PDK-1 as a central regulator and integrator of the
370 systemic and local metabolic reprogramming required for tissue repair.
371
372
373 **Discussion**
374
375 Our study provides insights into the local and systemic adaptations of metabolic processes during tissue
376 repair and regeneration (**Fig 6O,P**). Our findings distinguish adaptations in proliferating cells of the
377 regenerating domain from senescent or quiescent cells within damaged tissues. Here we show that the
378 behavior of quiescent-like cells distal to the site of inflammatory damage is characterized by reduced
379 protein synthesis and cell proliferation and correlates with a low insulin-signaling environment. Previous
380 work suggest that systemic growth restriction may prevent the progression and overgrowth of undamaged
381 tissues, thereby synchronizing regeneration with developmental progression (Cao et al, 2022; Colombani
382 et al, 2012; Garelli et al, 2012; Hackney & Cherbas, 2014; Halme et al, 2010).
383
384 Importantly, how the regenerating domain overcomes such a restrictive systemic environment was not
385 known. Here, we demonstrate that proliferating cells in *egr*-expressing wing discs display a distinct
386 upregulation of ribosomal S6 protein phosphorylation and maintain high levels of protein synthesis. A

387 domain characterized by ribosomal S6 protein phosphorylation was recently described in mouse and pig
388 skin wounds, implicating potential similarities in regenerative programs across species (Ring et al, 2023).
389 Besides mTORC1, PDK-1 and JNK can act as activators of S6K (Wu et al, 2022). Yet, JNK signaling in
390 proliferating cells of the regenerating domain is low. Our findings show that the PDK-1 kinase is essential
391 to support protein translation and growth during regeneration. PDK-1 is typically considered to be part of
392 the Insulin/AKT/FOXO; yet, in the regenerating domain, cells proliferate independent of Insulin/AKT/FOXO
393 activity. PDK-1 upregulation appears to act as a substitute compensating the lack of Insulin/AKT/FOXO
394 signaling and thus acts as an alternative driver of proliferative metabolism to support tissue repair. This
395 is supported by previous studies on AKT-independent but PDK-1-dependent growth during *Drosophila*
396 development (Radimerski et al, 2002; Rintelen et al, 2001). Given that PDK-1 may bypass a need for
397 Insulin/AKT/FOXO, it may not be surprising that PDK-1 upregulation is found in many cancers (Zheng et
398 al, 2023). In addition to S6K activity, Myc levels are elevated in the regenerating domain (Crucianelli et al,
399 2022; Smith-Bolton et al, 2009). The function of Myc as a positive regulator of ribosome biogenesis and
400 protein translation may thus further support growth and proliferation in this domain (Destefanis et al,
401 2020). In our study, we identify JAK/STAT signaling as an upstream regulator of PDK-1, phosphorylation of
402 ribosomal S6 protein, and protein synthesis. Our work thus uncovers a pathway whereby JAK/STAT
403 signaling mediates the known proliferation and survival-promoting function in imaginal disc
404 development, regeneration, and tumor growth (Herrera & Bach, 2019).
405
406 The increased expression of nutrient transporters in proliferating cells suggests that the regeneration
407 program allows for selective uptake of mobilized nutrients from the hemolymph environment. The
408 hemolymph from *egr*-expressing larvae exhibited enrichment of metabolites associated with glutamate
409 and arginine metabolism when compared to control larvae. Remarkably, the upregulation of both the urea
410 cycle metabolite ornithine in the hemolymph and the predicted ornithine-transporter CG5535 in the
411 regenerating domain suggest a role for urea cycle metabolism during regeneration. Prior research has
412 shown that dietary supplementation of ornithine significantly enhances wound healing parameters in
413 mice (Shi et al, 2002; Witte & Barbul, 2003). Earlier studies indicated elevated levels of ornithine,
414 glutamate, and glutamine in rat wound fluids (Albina et al, 1993). Our findings suggest that glutamate
415 metabolism may support regeneration, aligning with its described roles in tumor growth, inflammation,
416 and glutathione oxidative stress defenses (Altman et al, 2016; Ling et al, 2023; Zhu & Thompson, 2019).
417 By coupling glutaminolysis to the urea cycle, the proliferating cell would be able to channel nitrogen into
418 different metabolic processes such as non-essential amino acid (NEAA) synthesis via transamination,
419 thereby extending the advantages of urea cycle use beyond arginine, polyamines, or nitric oxide
420 production (Keshet et al, 2018).
421
422 Importantly, our study elucidates how wild type cells can proliferate and repair physiological
423 inflammation. The program systemically inhibits growth and proliferation and drives nutrient release form
424 energy-storing organs like the fat body. Undoubtedly, the systemic effects are part of an ancient and

425 conserved stress response and repair program designed to distribute nutrients from an energy store to
426 the site of tissue damage. Evolutionarily, this program would guarantee a nutrient supply to the
427 regenerating area and therefore prioritize repair, especially if feeding or foraging opportunities for the
428 organism may be scarce or limited by injuries. If activated more long-term by inflammatory pathologies,
429 like tumors, this program turns from a repair program to chronic cachexia and lethal organ wasting. While
430 oncogenic mutations may facilitate nutrient use in such a cachexic environment (Lee et al, 2021; Newton
431 et al, 2020; Santabarbara-Ruiz & Leopold, 2021; Song et al, 2019), our work reveals how normal tissue
432 adapts within the repair program to overcome the systemic inhibition of growth. Our work highlights the
433 JAK/STAT-PDK-1 and mTORC1 axis as crucial mediators of regenerative growth.
434

Materials and Methods

Drosophila maintenance

All experiments were performed on *Drosophila melanogaster*. Fly strains (see **Table S1**) were maintained on standard fly food (10L water, 74,5g agar, 243g dry yeast, 580g corn flour, 552ml molasses, 20.7g Nipagin, 35ml propionic acid) at 18°C – 22°C. Larvae from experimental crosses were allowed to feed on Bloomington formulation (175.7g Nutry-Fly,1100ml water 20g dry yeast, 1.45g Nipagin in 15ml Ethanol, 4.8ml Propionic acid) and raised at 18°C or 30°C to control GAL80ts-dependent induction of GAL4/UAS. Our experimental design did not consider differences between sexes unless for genetic crossing schemes.

Drosophila genetics

To induce expression of UAS-constructs, such as *UAS-egr*, under the control of rn-GAL4 in the wing pouch, experiments were carried out as described in (Cosolo et al, 2019; La Fortezza et al, 2016; Smith-Bolton et al, 2009) with minor modifications. Briefly, larvae of genotype *rn-GAL4, tub-GAL80^{ts}* and carrying the desired *UAS*-transgenes were staged with a 6h egg collection and raised at 18°C at a density of 50 larvae/vial. Overexpression of transgenes was induced by shifting the temperature to 30°C for 24h on the seventh day (D7) after egg deposition (AED) to relieve temperature-sensitive GAL80ts repression of GAL4. Larvae were dissected after 24 h of *egr*-expression. Control genotypes were generated by crossing *rn-GAL4, tub-GAL80^{ts}* into a wild type background.

Immunohistochemistry of wing imaginal discs

Wing discs from third instar larvae were dissected and fixed for 15 minutes at room temperature in 4% paraformaldehyde in PBS. Washes were performed in PBS containing 0.1% TritonX-100 (PBT). The discs were then incubated with primary antibodies (listed in **Table S2**) in 0.1% PBT, gently mixed overnight at 4°C. During incubation with cross-absorbed secondary antibodies coupled to Alexa Fluorophores at room temperature for 2 hours, tissues were counterstained with DAPI (0.25 ng/µL, Sigma, D9542). Tissues were mounted using SlowFade Gold Antifade (Invitrogen, S36936). To ensure comparability in staining between different genotypes, experimental and control discs were processed in the same vial and mounted on the same slides whenever possible. Images were acquired using the Leica TCS SP8 Microscope, using the same confocal settings for linked samples and processed using tools in Fiji.

Protein synthesis assays using OPP- Click-iT staining

OPP Assays were performed using Click-iT® Plus OPP Protein Synthesis Assay Kits (Invitrogen Molecular Probe) according to manufacturer's instructions. Briefly, larvae were dissected and inverted cuticles were incubated with a 1:1000 dilution of Component A in Schneider's medium for 15 minutes on a nutator. Larval cuticles were fixed with 4% paraformaldehyde for 15 minutes, rinsed twice in 0.1% PBT, and permeabilized with 0.5% PBT for 15 minutes. The cuticles were then stained with the Click-iT®

473 cocktail for 30 minutes at room temperature, protected from light. Further immunohistochemistry
474 analysis and sample mounting was performed as described above.
475
476 **EdU labelling**
477 EdU incorporation was performed using the Click-iT Plus EdU Alexa Fluor 647 Imaging Kit. Briefly, larval
478 cuticles were inverted in Schneider's medium and incubated with EdU (10μM final concentration) at RT
479 for 15 minutes. Cuticles were then fixed in 4% PFA/PBS for 15 minutes, washed for 30 minutes in PBT
480 0.5%. EdU-Click-iT labeling was performed according to manufacturer's guidelines. Further
481 immunohistochemistry analysis and sample mounting was performed as described above.
482
483 **SA-β-Gal staining**
484 Cell senescence detection kit from Invitrogen (C10850) was used to analyze senescence-associated β-
485 galactosidase activity. Briefly, larval cuticles were inverted in PBS, fixed with 4% PFA, washed with 1%
486 BSA (in PBS) and then incubated in working solution for 2h at 37°C, according to manufacturer's
487 instructions. Washing steps were performed in PBS and PBS containing 0.1% TritonX-100 (PBT). Further
488 immunohistochemistry analysis and sample mounting was performed as described above.
489
490 **Fat body Nile Red staining**
491 Early third instar larvae were collected in PBS and dissected, leaving the gut intact to prevent fat body
492 loss. Inverted cuticles were transferred to an Eppendorf tube and fixed with 4% paraformaldehyde/PBS
493 for 15 minutes. Samples were washed in 0.1% PBT. Cuticles were incubated with Nile Red (2 μg/mL in
494 PBS) for 1 hour, protected from light. Following incubation, samples were washed in PBS, the fat body
495 was dissected and mounted as described above.
496
497 **Hemolymph sample preparation**
498 Fifteen larvae were collected and thoroughly washed with Milli-Q water to remove any fly food particles.
499 Care was taken to ensure no food particles remained on the larvae surfaces, and they were dried using
500 Kim Tech paper wipes. Each larva was punctured in the center using forceps and transferred to a 0.5 mL
501 microcentrifuge tube with three 1 mm holes at the bottom. The 0.5 mL microcentrifuge tube was then
502 placed into a pre-cooled 1.5 mL microcentrifuge tube. One larva at a time was processed in this assembly
503 and centrifuged in a microfuge for 10 seconds. After each centrifugation, the larval carcass was removed
504 from the 0.5 mL microcentrifuge tube to prevent blockage of the holes. Hemolymph isolated from the 15
505 larvae was collected in the bottom 1.5 mL tube. From the total collected hemolymph, 8 μL was transferred
506 to a fresh 1.5 mL tube, and 10 μL of ultrapure Milli-Q water, 30 μL of methanol, an internal standard, and
507 50 μL of MTBE were added. The solution was mixed thoroughly and centrifuged at 1000g for 10 minutes at
508 4°C. After centrifugation, the organic and polar phases were collected separately in different tubes for
509 metabolite measurement.
510

511 **Hemolymph metabolomic analyses**

512 Non-targeted analysis of polar metabolites by LC-MS was carried out as described previously (Edwards-
513 Hicks et al, 2020) using an Agilent 1290 Infinity II UHPLC in line with a Bruker Impact II QTOF-MS operating
514 in negative and positive ion mode. Scan range was from 20 to 1050 Da and mass calibration was
515 performed at the beginning of each run. LC separation was on a Waters Atlantis Premier BEH ZHILIC
516 column (100 x 2.1 mm, 1.7 µm particles), buffer A was 20 mM ammonium carbonate and 5 µM medronic
517 acid in milliQ H2O and buffer B was 90:10 acetonitrile:buffer A and the solvent gradient was from 95% to
518 55% buffer B over 14 minutes. Flow rate was 180 µL/min, column temperature was 35 °C, autosampler
519 temperature was 5 °C and injection volume was 3 µL. Data processing including feature detection, feature
520 deconvolution, and annotation of features was performed using MetaboScape (version 2023b). Quantile
521 normalization was performed to minimize sample size effects and further statistical processing were
522 performed with R. Metabolites with missing values were eliminated from the dataset. Both, the Shapiro-
523 Wilk test and the Q-Q plot, showed that the data was not normally distributed. Therefore, a two-sided,
524 unpaired Wilcoxon rank-sum test was performed on the quantile normalized data. Only metabolites with
525 at least <0.75 and >1.5 fold change and a p-value < 0.19 and were selected for further analysis and were
526 displayed in a heatmap with row-wise normalization (Fig 3L).

527

528 **Image quantification and statistical analysis - General comments**

529 For all quantifications, control and experimental samples were processed together and imaged in
530 parallel, using the same confocal settings. Images were processed, analyzed and quantified using tools
531 in Fiji (ImageJ 2.14) (Schindelin et al, 2012). Extreme care was taken to apply consistent methods to
532 control and experimental samples (i.e., number of projected sections, thresholding methods,
533 processing) for image analysis and quantifications. See **File S1** for macros used in FIJI during image
534 segmentation and quantifications. Further details on segmentation and quantifications are provided
535 below. Figure panels were assembled using Affinity Designer 2.4.0. Statistical analyses were performed
536 in Graphpad Prism. Illustrations were done in Biorender.

537 To quantify fluorescence intensities inside the proliferative domain (PD^{egr}), a mask of the high JNK-
538 signaling domain region was generated, followed by creating a 20µm band on the outside to mark the
539 proliferative domain. Fluorescence intensities in proliferative domains was always compared to
540 fluorescence intensities within the pouch domain of control discs, unless otherwise noted.

541

542 **Quantification of cycling cells using EdU incorporation**

543

544 **(a) EdU quantification in notum:** An xy-section with the maximum number of notum epithelial cells was
545 selected, excluding any myoblast cells. A mask was created from the DAPI staining to represent nuclei
546 and saved as ROI. A binary operation (AND) was used to compute a notum DAPI mask with the aid of a
547 manually selected notum region (FileS1, Macro-1L(a)). This mask was then used to measure EdU
548 intensity.

549 **(b) EdU quantification within 10µm bands:** In *egr*-expressing discs, TRE-RFP expression was used to
550 generate a mask of the high JNK-signaling domain (FileS1, Macro-1D(a)). The boundary of this mask
551 defined the regions inside and outside the high JNK region. Five 10µm bands were created outside the
552 high JNK-signaling domain, and three 10µm bands inside of the JNK-signaling domain. Also applying a
553 DAPI mask to each band (FileS1, Macro-1D(b)), the mean EdU intensity in each of the 10µm bands was
554 measured. Consistent with previous studies (Cosolo et al, 2019; Jaiswal et al, 2023), the highest EdU
555 intensities were observed in 3 bands outside the JNK-signaling domain, which was denoted as
556 proliferative domain.
557 **(c) EdU quantification in eye disc:** For the eye disc, a DAPI mask (FileS1, Macro-2C(a)) was generated
558 using the DAPI staining, which was then applied to measure EdU intensity in the region above the
559 morphogenetic furrow. EdU intensity was also measured inside an EdU-based mask, which was
560 generated on a single X-Y slice.
561
562 **Quantification of Upd3-LacZ levels**
563 A maximum projection of TRE-RFP expression was used to generate a mask of the high JNK-signaling
564 domain in *egr*-expressing disc (FileS1, Macro-4J(a)). Upd3-LacZ intensity was measured within the TRE-
565 RFP mask of the high JNK-signaling domain in *egr*-expressing disc, while for the control disc, Upd3-LacZ
566 intensity was measured in the pouch.
567
568 **Quantification of ImpL2-GFP levels**
569 A pouch mask was generated using the maximum projection of an anti-Nubbin staining (FileS1, Macro-
570 4G(a)) for both control and *egr*-expressing discs. ImpL2-GFP intensities were measured within the Nubbin
571 mask on the sum projection of the ImpL2-GFP signals within the stack (seven slices in each disc).
572
573 **Quantification of OPP levels in different regions of wing imaginal disc**
574 In the control disc, mean OPP intensity was measured separately in the pouch, hinge, and notum regions.
575 In *egr*-expressing discs, mean OPP intensity was measured in the high JNK signaling region (TRE-RFP
576 mask), the proliferative region (20µm band around the TRE-RFP mask), and the notum region. In control
577 discs, the pouch, hinge, and notum regions were selected using wing fold landmarks. In *egr*-expressing
578 discs, a max projection of TRE-RFP intensities was used to create a mask of the high JNK signaling domain
579 (FileS1, Macro-1G(a)), which was applied to measure OPP intensity in the high JNK region. A 20µm band
580 outside the high JNK region was generated to mark the proliferative region, and OPP intensity in this
581 domain was measured. For the notum, a manual selection along the first notum fold and outlining the
582 edges of the notum was carried out.
583
584 **Quantification of OPP levels in the eye disc**

585 For the eye-antennal disc, the DAPI staining was used to generate a mask of the tissue outline (FileS1,
586 Macro-2F(a)) and combined with a manual selection of the eye disc to generate a region of interest (ROI)
587 within which we measured OPP intensity.
588
589 **Quantification of nuclear dFOXO levels**
590 In control discs, a slice with the maximum number of pouch cells was selected and a DAPI mask (FileS1,
591 Macro-5C(a)) was generated and combined with manual pouch selection to create a pouch nuclear
592 mask. This mask was used to measure mean dFOXO intensity in the pouch nucleus. In *egr*-expressing
593 discs, a single slice from the Z-stack with the maximum number of cells in the proliferative domain was
594 selected. A max projection of TRE-RFP intensities was used to create a mask of the high JNK signaling
595 domain, and a 20µm band was created to locate the proliferative region. A DAPI mask (FileS1, Macro-
596 5C(b)) was generated from the selected slice and combined with the 20µm band to create a new mask for
597 the proliferative cell nuclei, which was used to measure dFOXO intensity in the nucleus. Please note that
598 discs and fat body were treated with Leptomycin B (413nM) for 30 min before dissection to block nuclear
599 export.
600
601 **Quantification of PDK-1 GFP, p-S6 and OPP levels in the en-GAL4 domain**
602 The slice with the maximum number of pouch cells was selected, and masks of the anterior and posterior
603 pouch compartments were generated by segmenting the enGAL4, UAS-RFP expression domain. Levels of
604 p-S6 and Pdk1-GFP intensities were measured within these masks and the P/A ratio (en-GAL4 region/non-
605 en-GAL4 region) was calculated. Mean OPP intensity in the control and experimental pouch en-GAL4
606 domain was measured and reported.
607
608 **Quantification of 10xStat92E-GFP levels in the fat body**
609 A single slice from the Z-stack with the maximum number of nuclei was selected. A 200x200 pixel square
610 region was defined and used as a standard area for measurement of GFP intensities.
611
612 **Quantification of lipid droplet size and shape**
613 A single slice from the Z-stack through the most anterior fat body containing the maximum number of
614 nuclei was selected. A published STAR protocol was applied to measure lipid droplet area in both control
615 and experimental samples (https://doi.org/10.1016/j.xpro.2022.101230). Additionally, the roundness of
616 lipid droplets was measured using the same published workflow.
617

Author Contributions

Conceptualization AVM, AKC; Data curation AVM, LH, AKC; Formal analysis AVM, LN, LH, JB, AKC; Funding acquisition AKC; Investigation AVM, LN, AKC; Methodology AVM, LN, IG, JB, AKC; Project administration IG, AKC; Supervision KK, AKC; Validation AVM, LN, KK, AKC; Visualization AVM, LN, LH; Writing – original draft AVM, AKC; Writing – review & editing AVM, LN, KK, AKC

Acknowledgements

We thank the staff of the Life Imaging Center (LIC) in the Hilde Mangold House (HMH) of the Albert-Ludwigs-University of Freiburg for help with their confocal microscopy resources, and the excellent support in image recording. We specifically thank the DFG for supporting our imaging work through project number 414136422. We thank Susumi Hirobayashi, Hugo Stocker, Aurelio Teleman and Hong Xu, Iswar Hariharan, Dirk Bohmann for sharing reagents and the Bloomington *Drosophila* Stock Center (BDSC), the Vienna *Drosophila* Stock Collection (VDRC), the University of Zurich ORFeome Project (FlyORF), the Developmental Studies Hybridoma Bank (DSHB) and the Monoclonal Antibody Core Facility at the Helmholtz Zentrum Munich for providing fly stocks and antibodies. We thank the IMPRS-IE graduate school for supporting our doctoral researchers. We thank Olaf Gross and Valerie Hilgers for critical feed-back on the manuscript.

Funding

Funding for this work was provided by the Deutsche Forschungsgemeinschaft (DFG, German Research Foundation) under Germany ś Excellence Strategy (CIBSS – EXC-2189), the Heisenberg Program (CL490/3-1, CL490/4-1), and by the Boehringer Ingelheim Foundation (BIF Plus3 & Rise Up) to AKC. The funders had no role in study design, data collection and analysis, decision to publish, or preparation of the manuscript.

Declaration of Interest

The authors declare no competing interests.

Main Figures

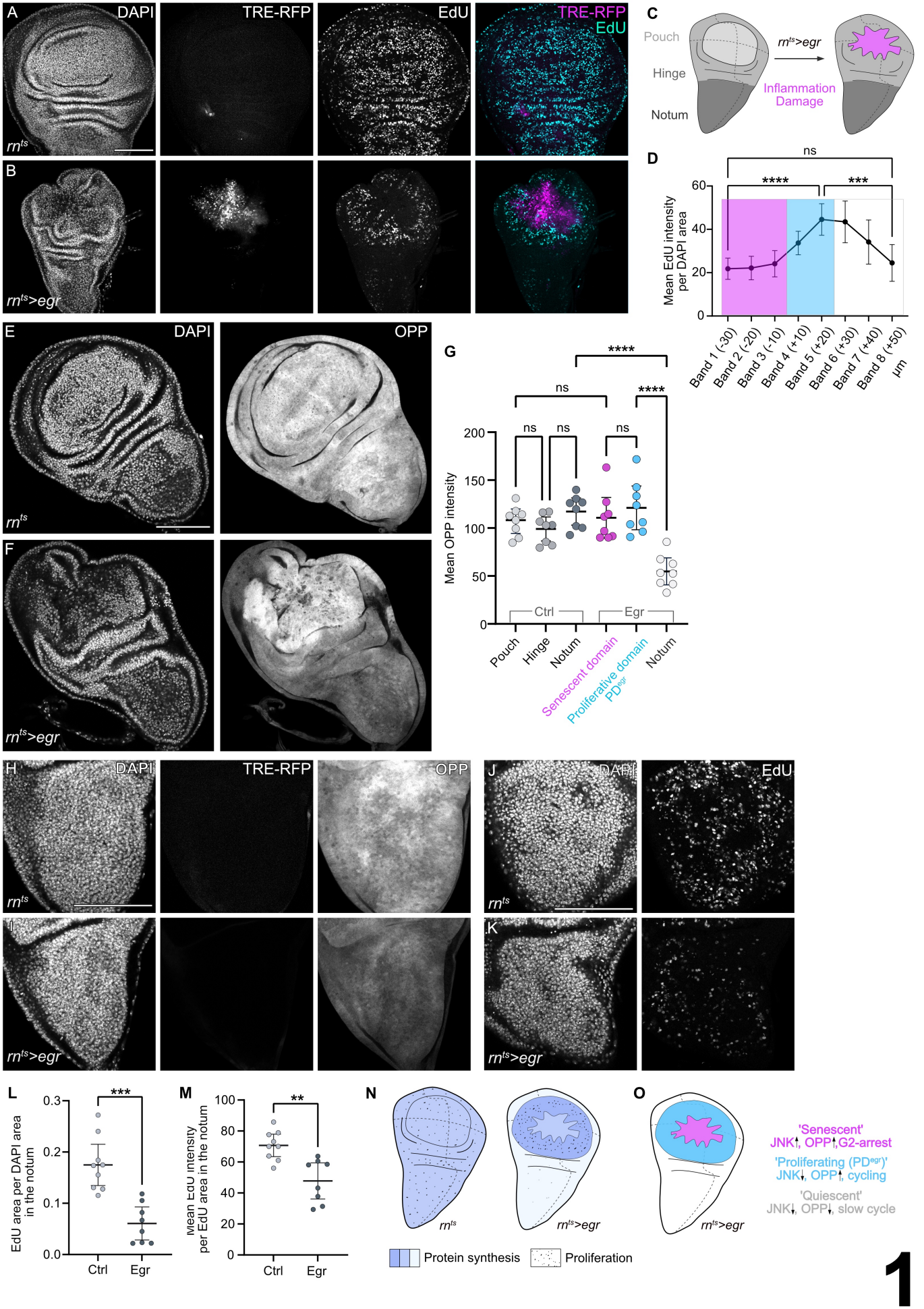
A
DAPI
TRE-RFP
EdU
TRE-RFP
EdU
rn^ts
B
rn^ts>egr
C
Pouch
Hinge
Notum
rn^ts>egr
Inflammation
Damage
D
ns
****
***
Mean EdU intensity per DAPI area
Band 1 (-30)
Band 2 (-20)
Band 3 (-10)
Band 4 (+10)
Band 5 (+20)
Band 6 (+30)
Band 7 (+40)
Band 8 (+50)
µm
E
DAPI
OPP
rn^ts
F
rn^ts>egr
G
Mean OPP intensity
Ctrl
Egr
Pouch
Hinge
Notum
Senescent domain
Proliferative domain
PD^egr
Notum
H
DAPI
TRE-RFP
OPP
rn^ts
I
rn^ts>egr
J
DAPI
EdU
rn^ts
K
rn^ts>egr
L
EdU area per DAPI area in the notum
Ctrl
Egr
M
Mean EdU intensity per EdU area in the notum
Ctrl
Egr
N
rn^ts
rn^ts>egr
Protein synthesis
Proliferation
O
rn^ts>egr
'Senescent'
JNK↑, OPP↑,G2-arrest
'Proliferating (PD^egr)'
JNK↓, OPP↑, cycling
'Quiescent'
JNK↓, OPP↓, slow cycle

1

652 **Figure 1. Spatial organization of cell proliferation and protein synthesis induced by inflammatory**
653 **damage in wing imaginal disc.**
654

655 **A,B.** Control wing disc (A) and a wing discs (B) after 24 hours of *egr*-expression within the wing pouch
656 domain (see Fig 1C) under the control of the rn-GAL4 driver (rn^{ts} and rn^{ts}>egr, respectively). TRE-RFP
657 visualizes JNK-pathway activity (magenta or grey) and EdU incorporation visualizes DNA replication (cyan
658 or grey). Discs were stained with DAPI to visualize nuclei.
659 **C.** Schematic representation of a third instar wing imaginal disc, highlighting different regions (pouch,
660 notum, and hinge) on the left. On the right, schematic representation of a wing imaginal disc after 24 hours
661 of *egr*-expression in the pouch. The magenta area identifies the JNK-signaling domain representing
662 inflammation and tissue damage.
663 **D.** Quantification of average EdU intensity in the DAPI area contained within 10μm bands segmented
664 inward and outward from the edge of the high JNK-signaling domain in *egr*-expressing discs. The the high
665 JNK-signaling domain is shaded in magenta, the proliferative domain marking the regenerating domain is
666 shaded in cyan. Mean and 95% CI (confidence interval) are shown. Statistical significance was tested
667 using a one-way ANOVA followed by Tukey's post-hoc test for multiple comparisons (n=7).
668 **E,F.** Protein synthesis visualized by O-proparyl-puromycin (OPP) incorporation into newly synthesized
669 proteins in control wing disc (E) and *egr*-expressing discs (F). Discs were stained with DAPI to visualize
670 nuclei.
671 **G.** Quantification of mean OPP intensity in three different regions of control and *egr*-expressing discs. In
672 control disc, OPP intensity was measured in the pouch, hinge, and notum, while in *egr*-expressing discs,
673 OPP intensity is measured in the high JNK signaling domain (approximating the central pouch), the
674 proliferating region (approximating the peripheral pouch and hinge), and the notum. Mean and 95% CI are
675 shown. Statistical significance was tested using a one-way ANOVA followed by Tukey's post-hoc test for
676 multiple comparisons (control: n=8, *egr*-expressing disc: n=8).
677 **H, I.** Protein synthesis visualized by OPP incorporation in the notum of control (H) and *egr*-expressing
678 discs (I).
679 **J,K.** EdU incorporation to visualize DNA replication in the notum of control (J) and *egr*-expressing discs
680 (K).
681 **L.** EdU area per DAPI area quantified in the notum of control and *egr*-expressing discs, serving as a proxy
682 for the number of cells undergoing DNA replication. Mean and 95% CI are shown. Statistical significance
683 was tested using an Unpaired t-test (control: n=9, *egr*-expressing disc: n=8), with a p-value = 0.0001.
684 **M.** Mean EdU intensity per EdU-positive area quantified in the notum of control and *egr*-expressing discs,
685 serving as a proxy for DNA replication speed. Mean and 95% CI are shown. Statistical significance was
686 tested using an Unpaired t-test (control: n=9, *egr*-expressing disc: n=8), with a p-value = 0.0011.
687 **N,O.** Schematic representation of protein synthesis rates (blue shades) and mitotic activity (black dots)
688 in control disc (left) and *egr*-expressing discs (right) (N). Based on activation of distinct signaling

689 pathways, or metabolic and mitotic activities in *egr*-expressing discs, three different cell populations
690 (senescent, proliferating and quiescent) can be distinguished (O).
691
692 Scale bars: 100 μm. Fluorescence intensities are reported as arbitrary units.

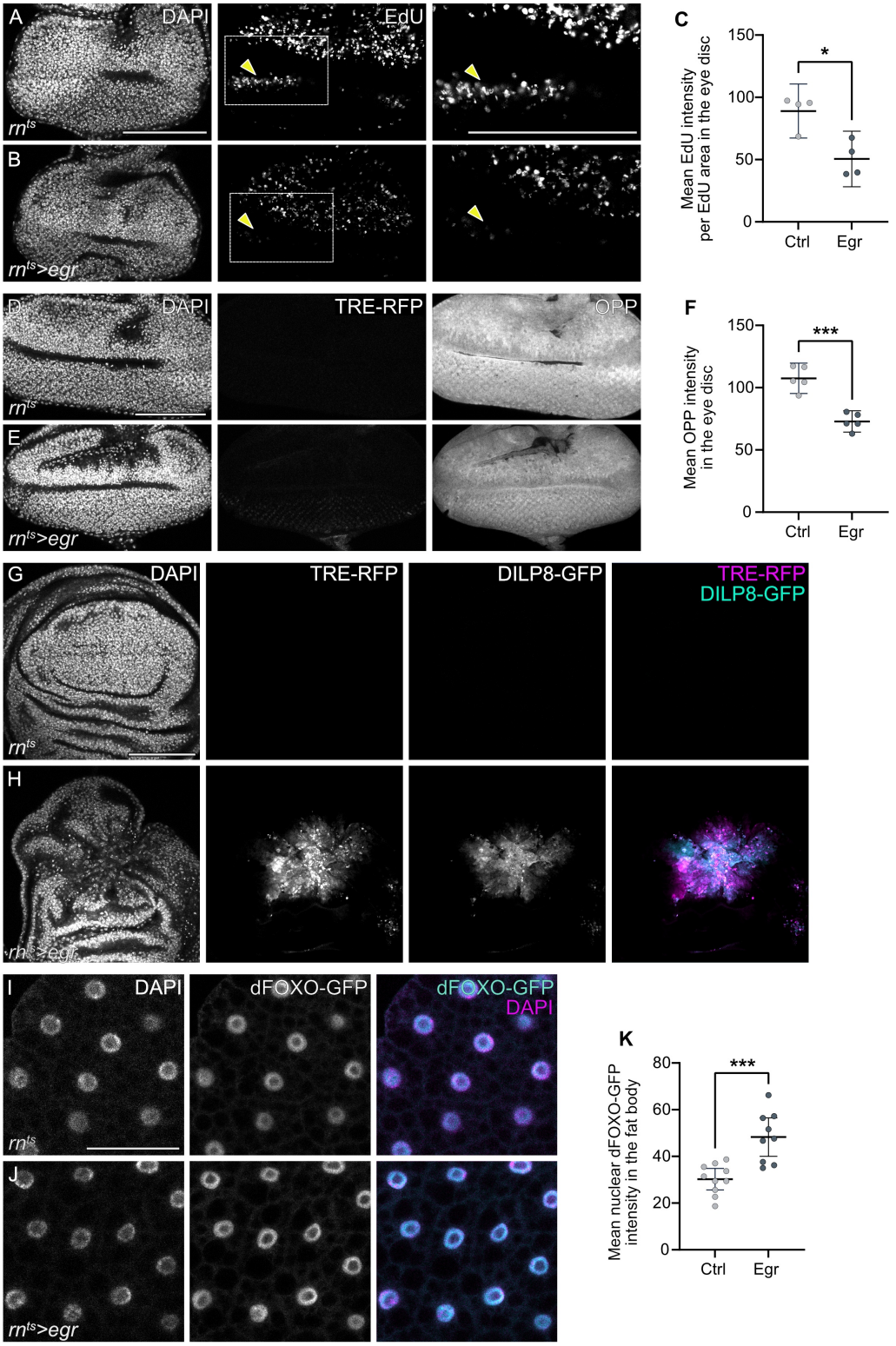
A
DAPI
EdU
rn^ts
B
rn^ts>egr
C
Mean EdU intensity per EdU area in the eye disc
150
100
50
0
*
Ctrl
Egr
D
DAPI
TRE-RFP
OPP
rn^ts
E
rn^ts>egr
F
Mean OPP intensity in the eye disc
150
100
50
0
***
Ctrl
Egr
G
DAPI
TRE-RFP
DILP8-GFP
TRE-RFP
DILP8-GFP
rn^ts
H
rn^ts>egr
I
DAPI
dFOXO-GFP
dFOXO-GFP
DAPI
rn^ts
J
rn^ts>egr
K
Mean nuclear dFOXO-GFP intensity in the fat body
80
60
40
20
0
***
Ctrl
Egr

2

Figure 2. Inflammatory tissue damage induces a systemic reduction in growth and cell proliferation.

A,B. EdU incorporation to visualizes DNA replication in eye imaginal discs, dissected from larvae with control (A) or *egr*-expressing (B) wing imaginal discs. The yellow arrowhead points to the expected location of the mitotic wave just anterior to the morphogenetic furrow.

C. Mean EdU intensity per EdU-positive area serving as a proxy for DNA replication speed, quantified in eye imaginal discs dissected from larvae with control or *egr*-expressing wing imaginal discs. Mean and 95% CI are shown. Statistical significance was tested using the Mann-Whitney test, p-value = 0.0286 (control: n=4, *egr*-expressing disc: n=4).

D,E. Protein synthesis visualized by OPP incorporation in the eye imaginal disc, dissected from larvae with control (D) or *egr*-expressing (E) wing imaginal discs. TRE-RFP visualizes JNK-pathway activity.

F. Mean OPP intensity in eye imaginal discs, dissected from larvae with control or *egr*-expressing wing imaginal discs. Mean and 95% CI are shown. Statistical significance was tested using an Unpaired t-test, p-value = 0.0002 (control: n=5, *egr*-expressing disc: n=5).

G,H. Expression of Dilp8-GFP (cyan or grey) in control (G) and *egr*-expressing discs (H). TRE-RFP visualizes JNK-pathway activity (magenta or grey). Discs were stained with DAPI to visualize nuclei.

I,J. Expression of dFOXO-GFP (cyan or grey) in fat body, dissected from larvae with control (I) or *egr*-expressing (J) wing imaginal discs. Fat bodies were stained with DAPI to visualize nuclei (magenta or grey).

K. Mean nuclear dFOXO-GFP intensity in fat body, dissected from larvae with control or *egr*-expressing wing imaginal discs. Statistical significance was tested using an unpaired t-test, p-value = 0.0003 (control: n=10, *egr*-expressing disc: n=9).

Scale bars: 100 μm. Fluorescence intensities are reported as arbitrary units.

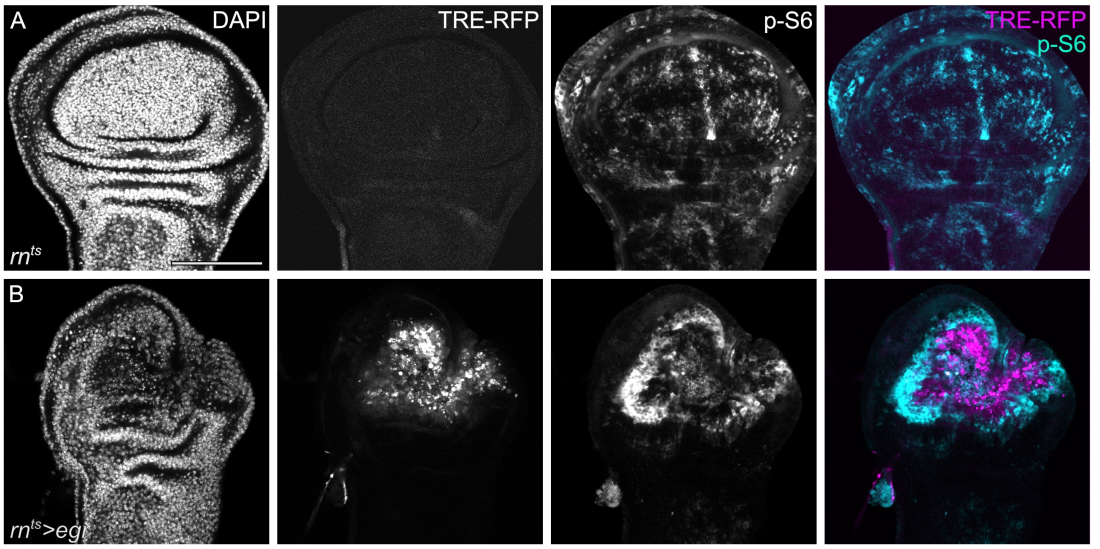
A
DAPI
TRE-RFP
p-S6
TRE-RFP
p-S6
rn^ts
B
rn^ts>egr

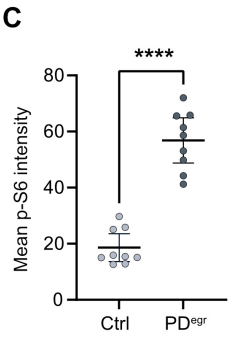
C
****
Mean p-S6 intensity
80
60
40
20
0
Ctrl
PD^egr

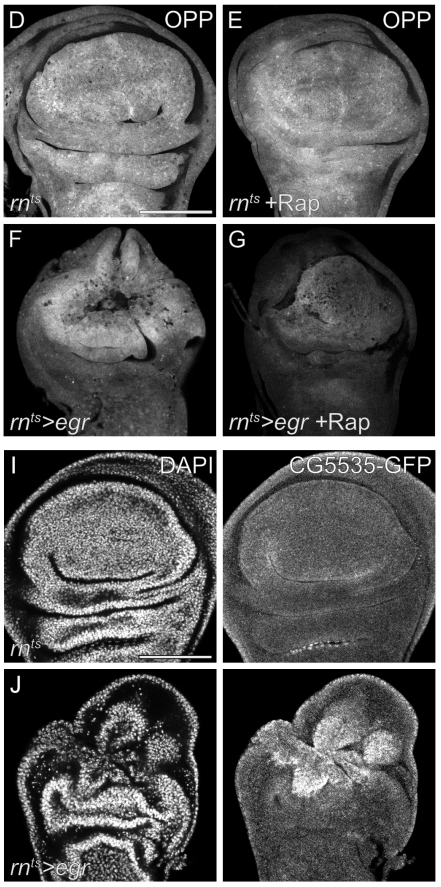
D
OPP
rn^ts
E
OPP
rn^ts +Rap
F
rn^ts>egr
G
rn^ts>egr +Rap
I
DAPI
CG5535-GFP
rn^ts
J
rn^ts>egr

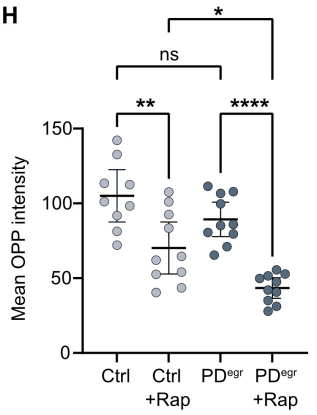
H
*
ns
**
****
Mean OPP intensity
150
100
50
0
Ctrl
Ctrl +Rap
PD^egr
PD^egr +Rap

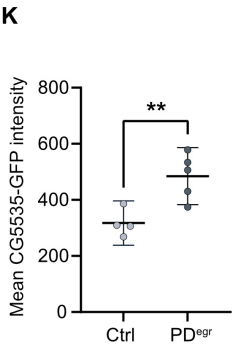
K
**
Mean CG5535-GFP intensity
800
600
400
200
0
Ctrl
PD^egr

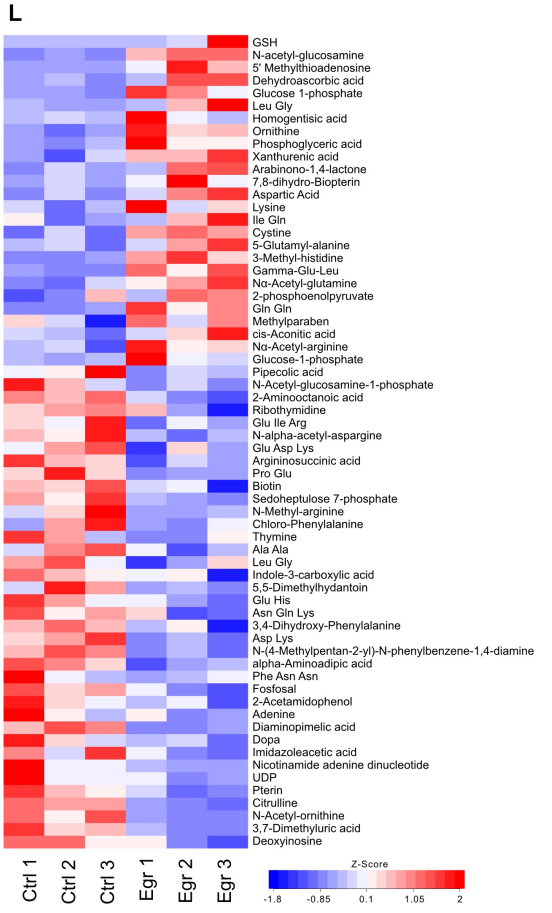
L
GSH
N-acetyl-glucosamine
5' Methylthioadenosine
Dehydroascorbic acid
Glucose 1-phosphate
Leu Gly
Homogentisic acid
Ornithine
Phosphoglyceric acid
Xanthurenic acid
Arabinono-1,4-lactone
7,8-dihydro-Biopterin
Aspartic Acid
Lysine
Ile Gln
Cystine
5-Glutamyl-alanine
3-Methyl-histidine
Gamma-Glu-Leu
Nα-Acetyl-glutamine
2-phosphoenolpyruvate
Gln Gln
Methylparaben
cis-Aconitic acid
Nα-Acetyl-arginine
Glucose-1-phosphate
Pipecolic acid
N-Acetyl-glucosamine-1-phosphate
2-Aminooctanoic acid
Ribothymidine
Glu Ile Arg
N-alpha-acetyl-aspargine
Glu Asp Lys
Argininosuccinic acid
Pro Glu
Biotin
Sedoheptulose 7-phosphate
N-Methyl-arginine
Chloro-Phenylalanine
Thymine
Ala Ala
Leu Gly
Indole-3-carboxylic acid
5,5-Dimethylhydantoin
Glu His
Asn Gln Lys
3,4-Dihydroxy-Phenylalanine
Asp Lys
N-(4-Methylpentan-2-yl)-N-phenylbenzene-1,4-diamine
alpha-Aminoadipic acid
Phe Asn Asn
Fosfosal
2-Acetamidophenol
Adenine
Diaminopimelic acid
Dopa
Imidazoleacetic acid
Nicotinamide adenine dinucleotide
UDP
Pterin
Citrulline
N-Acetyl-ornithine
3,7-Dimethyluric acid
Deoxyinosine
Ctrl 1
Ctrl 2
Ctrl 3
Egr 1
Egr 2
Egr 3
Z-Score
-1.8
-0.85
0.1
1.05
2

716 **Figure 3. mTORC signaling, nutrient transporters and metabolite changes in the hemolymph support**
717 **regenerative proliferation**

718

719 **A,B.** Immunostaining for phosphorylated-S6 (pS6, cyan or grey) in control (A) and *egr*-expressing discs (B).
720 TRE-RFP visualizes JNK-pathway activity (magenta or grey). Discs were stained with DAPI to visualize
721 nuclei.
722 **C**. Mean p-S6 intensity quantified in the pouch of control discs and the proliferative domain of *egr*-
723 expressing discs (PD^{egr}). Mean and 95% CI are shown. Statistical significance was tested using the Mann-
724 Whitney test, p-value = 0.0001 (control: n=9, *egr*-expressing discs: n=9).
725 **D-G.** Protein synthesis visualized by OPP incorporation in control (D,E) and *egr*-expressing discs (F,G)
726 from larvae fed on food without (D,F) or with rapamycin (200 μM) (E,G) for 24 h during the 24 h period of
727 *egr*-expression in wing discs.
728 **H.** Quantification of mean OPP intensity in the pouch of control discs and the proliferative domain of *egr*-
729 expressing discs (PD^{egr}) from larvae fed on food without or with rapamycin (200 μM) for 24 hours during
730 the 24 h period of *egr*-expression in wing discs. Mean and 95% CI are shown. Statistical significance was
731 tested using a one-way ANOVA followed by Tukey's post-hoc test for multiple comparisons (control: non-
732 fed:n=9, fed: n=10 ; *egr*-expressing disc: non-fed: n=10, fed: n=10).
733 **I,J.** Expression of CG5535-GFP in control (I) and *egr*-expressing discs (J). Discs were stained with DAPI to
734 visualize nuclei.
735 **K.** Mean CG5535-GFP intensity quantified in the pouch of control discs and the proliferative domain of
736 *egr*-expressing discs (PD^{egr}). Mean and 95% CI are shown. Statistical significance was tested using the
737 Unpaired t-test, p-value = 0.0092 (control: n=4, *egr*-expressing discs: n=5).
738 **L.** Heat map representing relative concentration changes of metabolites identified in the larval
739 hemolymph isolated from control larvae and *egr*-expressing larvae. The heat map was generated using
740 quantile normalized data, and statistical analysis was performed using a two-sided, unpaired Wilcoxon
741 rank-sum test (see Materials and Methods) and metabolites with at least <0.75 and >1.5 fold change were
742 selected for further analysis. Metabolites in the heat map are ordered based on the log2 fold change
743 between control and *egr*-expressing larval samples and Z-scores were visualized. Sample size was n=3
744 for both control and *egr*-expressing larvae.

745

746 Scale bars: 100 μm. Fluorescence intensities are reported as arbitrary units.

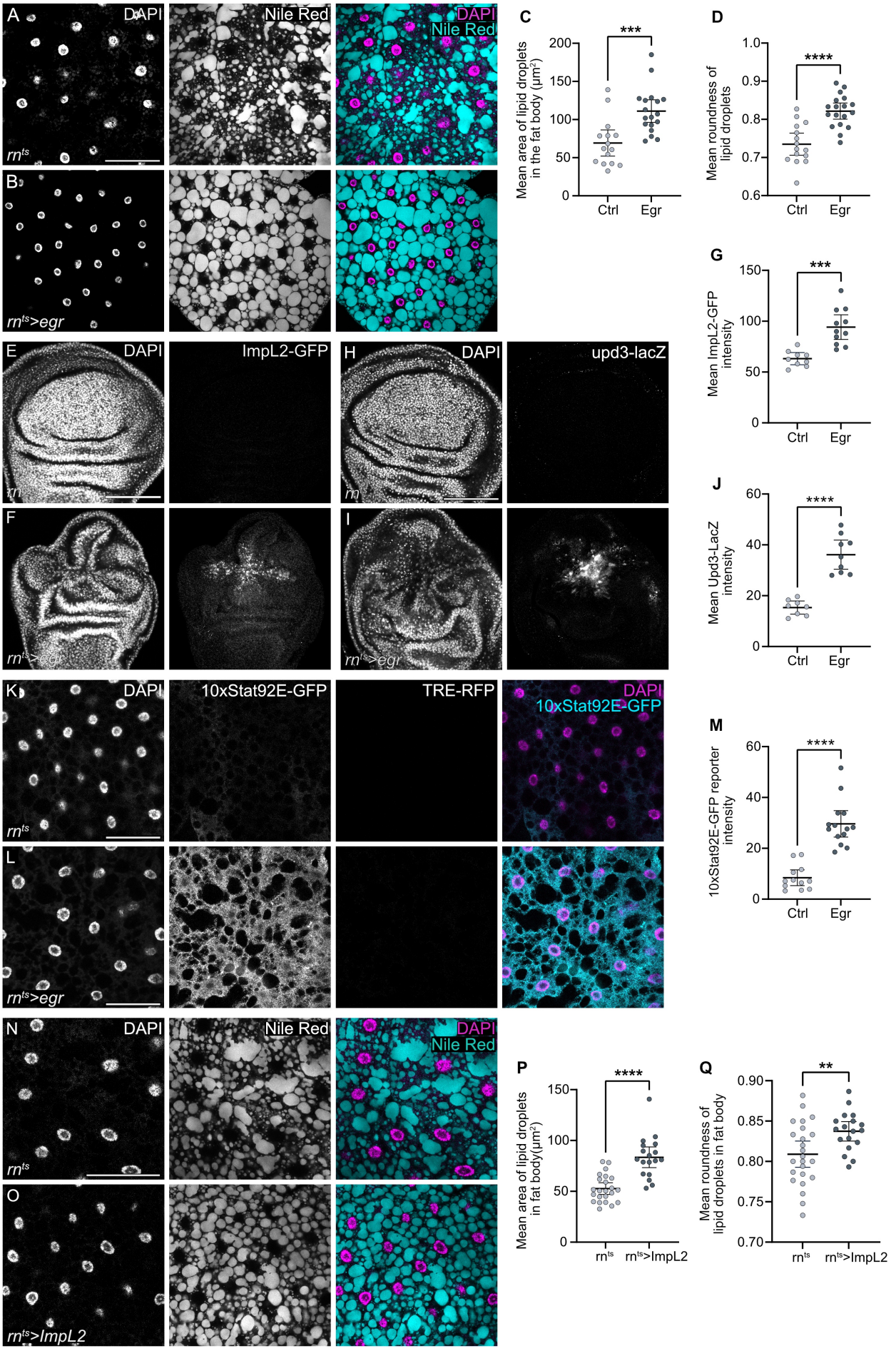
A
DAPI
Nile Red
DAPI
Nile Red
rn^ts
B
rn^ts>egr
C
***
Mean area of lipid droplets in the fat body (μm²)
200
150
100
50
0
Ctrl
Egr
D
****
Mean roundness of lipid droplets
1.0
0.9
0.8
0.7
0.6
Ctrl
Egr
E
DAPI
ImpL2-GFP
rn
F
rn^ts>egr
G
***
Mean ImpL2-GFP intensity
150
100
50
0
Ctrl
Egr
H
DAPI
upd3-lacZ
rn
I
rn^ts>egr
J
****
Mean Upd3-LacZ intensity
60
40
20
0
Ctrl
Egr
K
DAPI
10xStat92E-GFP
TRE-RFP
DAPI
10xStat92E-GFP
rn^ts
L
rn^ts>egr
M
****
10xStat92E-GFP reporter intensity
60
40
20
0
Ctrl
Egr
N
DAPI
Nile Red
DAPI
Nile Red
rn^ts
O
rn^ts>ImpL2
P
****
Mean area of lipid droplets in fat body(μm²)
150
100
50
0
rn^ts
rn^ts>ImpL2
Q
**
Mean roundness of lipid droplets in fat body
0.90
0.85
0.80
0.75
0.70
rn^ts
rn^ts>ImpL2

4

Figure 4. Impl2 signaling mobilizes nutrients in the fat body

A,B. Nile Red staining (cyan or grey) of fat body, dissected from larvae with control (A) or *egr*-expressing (B) wing imaginal discs. Fat bodies were stained with DAPI (magenta or grey) to visualize nuclei.

C, D. Quantification of area and roundness of lipid droplets in the fat body dissected from larvae with control (C) or *egr*-expressing (D) wing imaginal discs. Mean and 95% CI are shown. Statistical significance of was tested using an Unpaired t-test. Mean area, p-value = 0.0004. Mean roundness, p-value < 0.0001. (control: n=15, *egr*-expression in discs: n=18).

E,F. Expression of Impl2-GFP in control (A) and *egr*-expressing discs (B). Discs were stained with DAPI to visualize nuclei.

G,J. Impl2-GFP (G) and Upd3-lacZ (J) intensity quantified in the pouch of control wing discs and in the JNK-signaling domain of *egr*-expressing discs. Mean and 95% CI are shown and statistical significance was tested using Welch's t-test (Impl2-GFP: control: n=9, *egr*-expressing discs: n=11, p-value = 0.0001; Upd3-LacZ: control: n=8, *egr*-expressing disc: n=9, p-value < 0.0001).

H,I. Expression of Upd3-lacZ in control (C) and *egr*-expressing discs (D). Discs were stained with DAPI to visualize nuclei.

K,L. Activity of the JAK/STAT reporter *10xSTAT92E>GFP* (cyan or grey) in the fat body dissected from larvae with control (K) or *egr*-expressing (L) wing imaginal discs. TRE-RFP visualizes JNK-pathway activity (grey) and DAPI visualizes nuclei (magenta or grey).

M. Quantification of *10xSTAT92E>GFP* reporter intensity in the fat body dissected from larvae with control or *egr*-expressing wing imaginal discs. Mean and 95% CI are shown and statistical significance was tested using the Mann-Whitney test, p-value < 0.0001 (control: n=12, *egr*-expression in disc: n=14).

N,O. Nile Red staining of fat body, dissected from larvae with control (N) or Impl2-expressing (O) wing imaginal discs. Fat bodies were stained with DAPI to visualize nuclei.

P,Q. Quantification of area of lipid droplets and roundness of lipid droplets in the fat body dissected from larvae with either control discs or wing imaginal discs expressing ImpL2 for 24 h under the control of rn-GAL4. For lipid droplet area, statistical significance was tested using the Mann-Whitney test, p-value < 0.0001 (control: n=23, experiment: n=18). For lipid droplet roundness, statistical significance was tested using the Unpaired t-test, p-value=0.0088 (control: n=24, *egr*-expression in disc: n=18)

Scale bars: 100 μm. Fluorescence intensities are reported as arbitrary units.

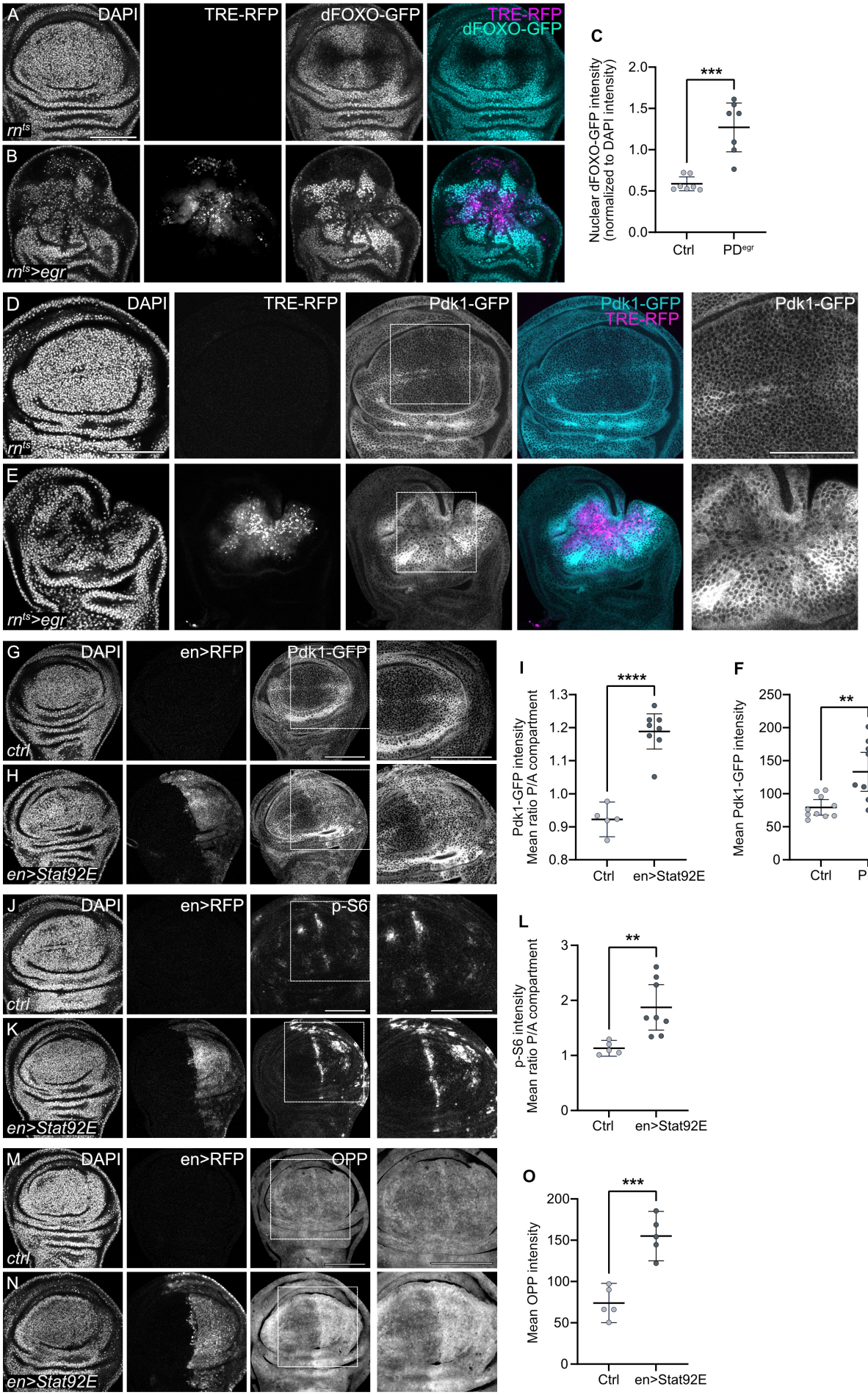
A
DAPI
TRE-RFP
dFOXO-GFP
TRE-RFP
dFOXO-GFP
rn^ts
B
rn^ts>egr
C
Nuclear dFOXO-GFP intensity
(normalized to DAPI intensity)
2.0
1.5
1.0
0.5
0.0
***
Ctrl
PD^egr
D
DAPI
TRE-RFP
Pdk1-GFP
Pdk1-GFP
TRE-RFP
Pdk1-GFP
rn^ts
E
rn^ts>egr
G
DAPI
en>RFP
Pdk1-GFP
ctrl
H
en>Stat92E
I
Pdk1-GFP intensity
Mean ratio P/A compartment
1.3
1.2
1.1
1.0
0.9
0.8
****
Ctrl
en>Stat92E
F
Mean Pdk1-GFP intensity
250
200
150
100
50
0
**
Ctrl
PD^egr
J
DAPI
en>RFP
p-S6
ctrl
K
en>Stat92E
L
p-S6 intensity
Mean ratio P/A compartment
3
2
1
0
**
Ctrl
en>Stat92E
M
DAPI
en>RFP
OPP
ctrl
N
en>Stat92E
O
Mean OPP intensity
200
150
100
50
0
***
Ctrl
en>Stat92E

5

Figure 5. STAT signaling regulates protein synthesis via regulation of Pdk1

A,B. Expression of dFOXO-GFP (cyan or grey) in control (A) and *egr*-expressing discs (B). TRE-RFP visualizes JNK-pathway activity (magenta or grey) and DAPI visualizes nuclei (grey).

C. Mean nuclear dFOXO-GFP intensity quantified in the pouch of control discs or the proliferative domain of *egr*-expressing discs (PD^{egr}). Mean and 95% CI are shown and statistical significance was tested using the Mann-Whitney test, p-value = 0.0006 (control: n=7, *egr*-expressing disc: n=7).

D,E. Expression of Pdk1-GFP (cyan or grey) in control (D) and *egr*-expressing discs (E). TRE-RFP visualizes JNK-pathway activity (magenta or grey) and DAPI visualizes nuclei (grey).

F. Quantification of Pdk1-GFP intensity in the pouch of control discs or the proliferative domain of *egr*-expressing discs (PD^{egr}). Statistical significance was tested using a Welch's t-test, p-value = 0.0025 (control: n=10, *egr*-expressing disc: n=10).

G-N. Control wing imaginal discs from sibling larvae (G,J,M) and wing imaginal discs expressing UAS-STAT92E in the posterior compartment under the control en-GAL4 which also drives expression of UAS-RFP (H,K,N). Discs were assayed for expression of Pdk1-GFP (G,H), levels of p-S6 (J,K), and protein synthesis using OPP incorporation assays (M,N). DAPI staining visualizes nuclei.

I,L,O. Quantifications of levels of Pdk1-GFP (I), p-S6 (L) and protein synthesis using OPP incorporation assays (O) in control wing imaginal discs and wing imaginal discs expressing UAS-STAT92E in the posterior compartment under the control en-GAL4. In the graph displaying Pdk1-GFP intensity (I), statistical significance was tested using the Unpaired t-test, p-value < 0.0001 (control: n=5, experiment: n=8). In the graph displaying p-S6 intensity (L), statistical significance was tested using Welch's t-test, p-value = 0.0033 (control: n=5, experiment: n=8). In the graph displaying OPP intensity (O), statistical significance was tested using the Unpaired t-test, p-value = 0.0004 (control: n=5, experiment: n=5). Mean and 95% CI are shown.

Scale bars: 100 μm. Fluorescence intensities are reported as arbitrary units.

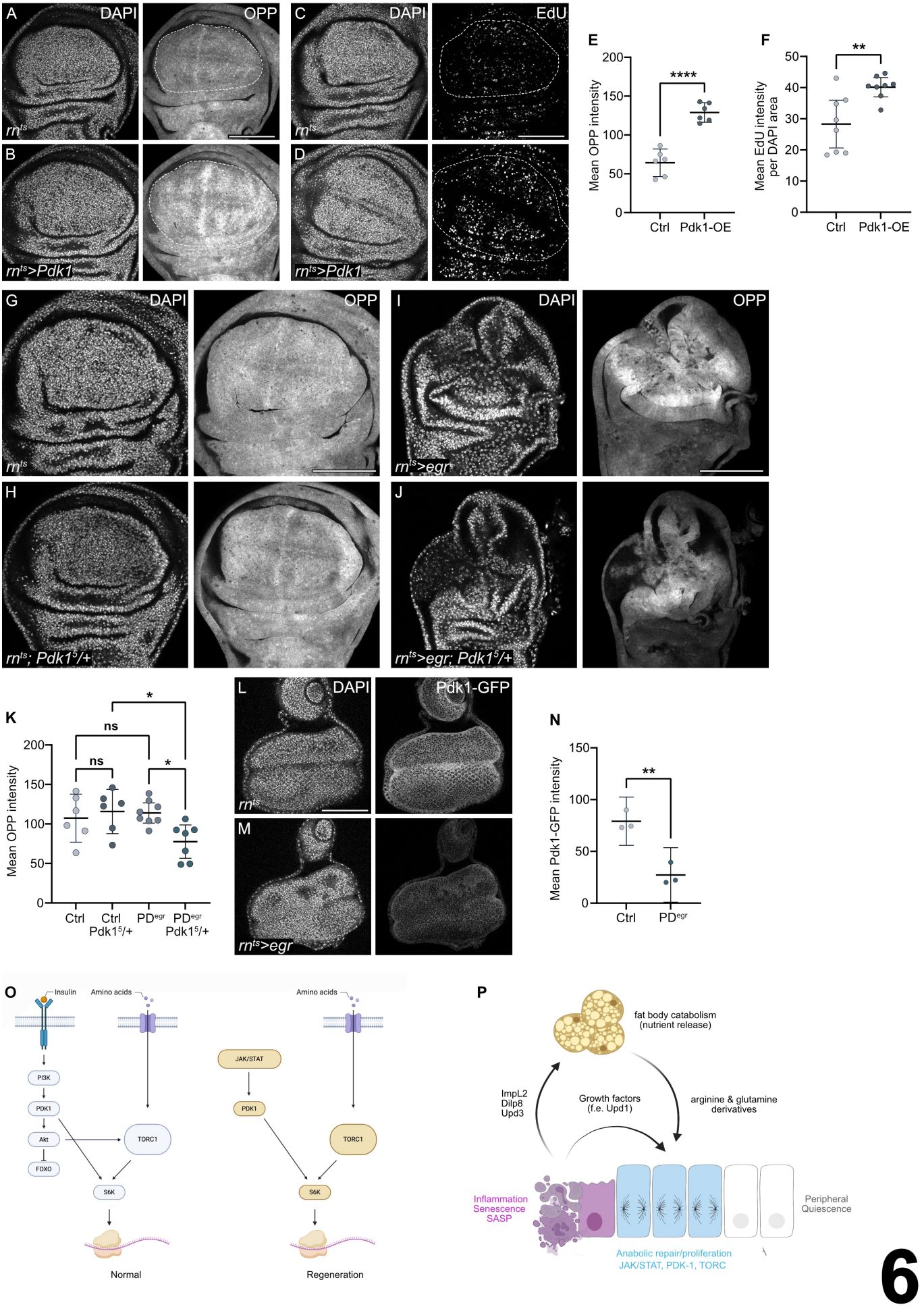
A
DAPI
OPP
rn^ts
B
rn^ts>Pdk1
C
DAPI
EdU
rn^ts
D
rn^ts>Pdk1
E
Mean OPP intensity
****
Ctrl
Pdk1-OE
F
Mean EdU intensity per DAPI area
**
Ctrl
Pdk1-OE
G
DAPI
OPP
rn^ts
I
DAPI
OPP
rn^ts>egr
H
rn^ts; Pdk1^5/+
J
rn^ts>egr; Pdk1^5/+
K
Mean OPP intensity
ns
ns
*
*
Ctrl
Ctrl Pdk1^5/+
PD^egr
PD^egr Pdk1^5/+
L
DAPI
Pdk1-GFP
rn^ts
M
rn^ts>egr
N
Mean Pdk1-GFP intensity
**
Ctrl
PD^egr
O
Insulin
Amino acids
PI3K
PDK1
Akt
FOXO
TORC1
S6K
Normal
Amino acids
JAK/STAT
PDK1
TORC1
S6K
Regeneration
P
fat body catabolism (nutrient release)
ImpL2
Dilp8
Upd3
Growth factors (f.e. Upd1)
arginine & glutamine derivatives
Inflammation
Senescence
SASP
Peripheral Quiescence
Anabolic repair/proliferation
JAK/STAT, PDK-1, TORC

806 **Figure 6. Pdk1 is a central regulator of regenerative metabolism**

807

808 **A,B.** Protein synthesis visualized by OPP incorporation in control discs (A) and discs expressing UAS-
809 PDK1 for 24 h under the control of rn-GAL4 (B). DAPI staining visualizes nuclei. The dotted white line
810 indicates the boundary of the wing pouch based on landmark tissue folds, approximating the rn-GAL4
811 expression domain.
812 **C,D.** EdU incorporation in control (C) and discs expressing UAS-PDK1 for 24 h under the control of rn-
813 GAL4 (D). DAPI staining visualizes nuclei. The dotted white line indicates the boundary of the wing pouch
814 based on landmark tissue folds, approximating the rn-GAL4 expression domain.
815 **E.** Quantification of mean OPP intensity in the pouch of control or *Pdk1*-expressing wing discs. Mean and
816 95% CI are shown and statistical significance was tested using an Unpaired t-test, p-value < 0.0001
817 (control: n=6, *Pdk1*-expressing disc: n=6).
818 **F.** Quantification of Mean EdU intensity per EdU-positive area serving as a proxy for DNA replication
819 speed, in the pouch of control or *Pdk1*-expressing wing discs. Mean and 95% CI are shown. Statistical
820 significance was tested using the Welch's t-test, p-value = 0.0078 (control: n=8, *Pdk1*-expressing disc:
821 n=8).
822 **G-J.** Protein synthesis visualized by OPP incorporation in control (G, H) and *egr*-expressing discs (I, J) that
823 were either wild type (G, I) or heterozygous mutant for the $Pdk1^5$ null allele (H, J). DAPI staining visualizes
824 nuclei.
825 **K.** Quantification of mean OPP intensity in the pouch of control or the proliferative domain of *egr*-
826 expressing discs (PD^{egr}) that were either wild type or heterozygous mutant for the $Pdk1^5$ null allele.
827 Statistical significance was tested using a one-way ANOVA followed by Tukey's post-hoc test for multiple
828 comparisons. (control:n=6, control, $PDK1^5$/+: n=6 ; *egr*:n=8, *egr*, $PDK1^5$/+: n=7).
829 **L, M.** Pdk1-GFP expression in eye imaginal discs, dissected from larvae with control or *egr*-expressing
830 wing imaginal discs. DAPI staining visualizes nuclei.
831 **N.** Quantifications of Pdk1-GFP expression in eye imaginal discs, dissected from larvae with control or
832 *egr*-expressing wing imaginal discs. Mean and 95% CI are shown. Statistical significance was tested using
833 an Unpaired t-test, p-value = 0.0031 (control: n=3, *egr*-expressing disc: n=3).
834 **O, P.** A model illustrating the local (O) and systemic (P) changes associated with anabolic growth and
835 protein synthesis in normal tissues (O, left) and in the regenerating domain within an insulin-restricited
836 environment. (O, right). Inflammatory cytokine signals (P) induce systemic changes that specifically
837 support metabolic adaptations for rapid proliferation during regeneration.
838 Scale bars: 100 µm. Fluorescence intensities are reported as arbitrary units.
839
840

Supplementary Figures and Tables

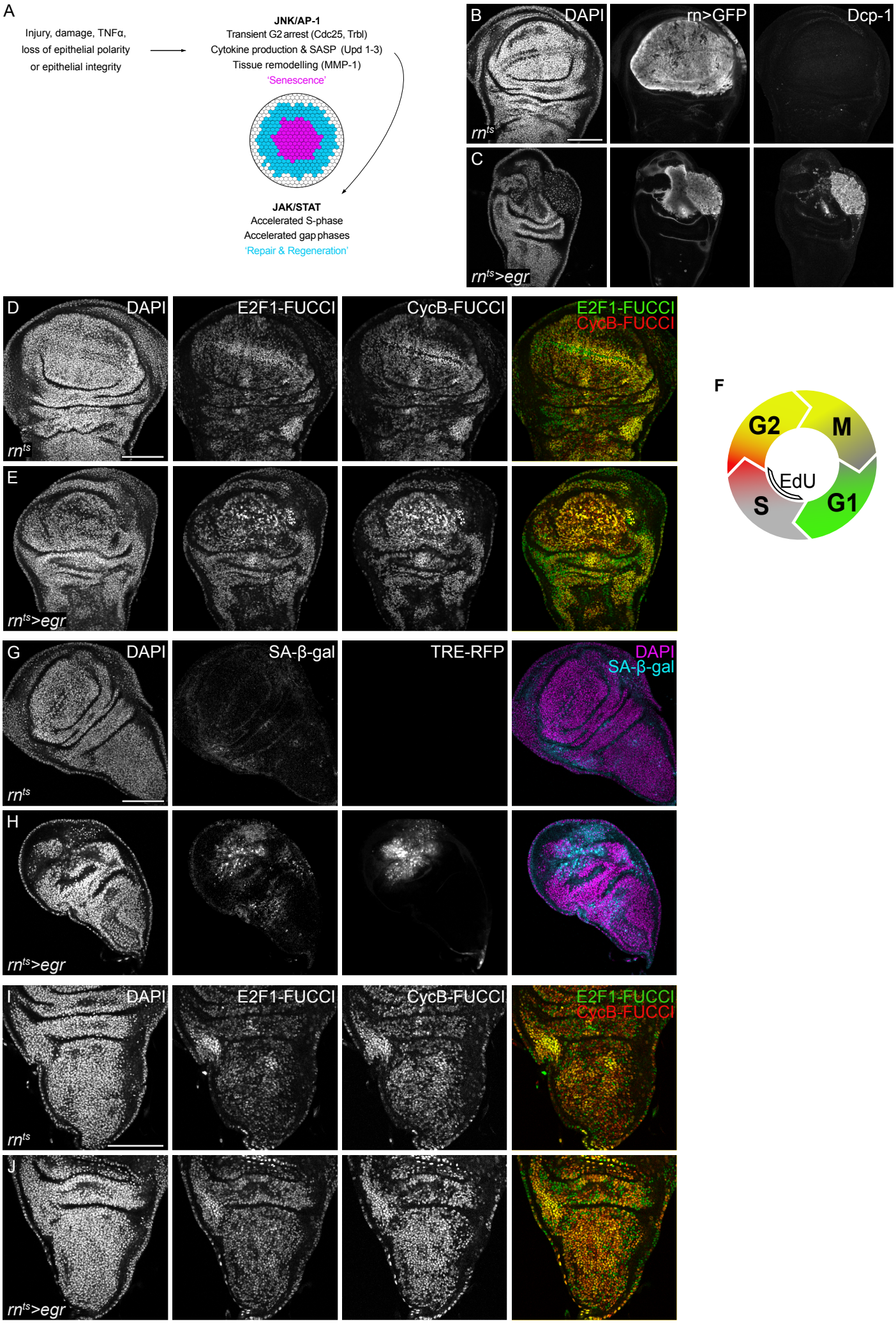
A
Injury, damage, TNFα,
loss of epithelial polarity
or epithelial integrity
JNK/AP-1
Transient G2 arrest (Cdc25, Trbl)
Cytokine production & SASP (Upd 1-3)
Tissue remodelling (MMP-1)
'Senescence'
JAK/STAT
Accelerated S-phase
Accelerated gap phases
'Repair & Regeneration'
B
DAPI
rn>GFP
Dcp-1
rnts
C
rnts>egr
D
DAPI
E2F1-FUCCI
CycB-FUCCI
E2F1-FUCCI
CycB-FUCCI
rnts
E
rnts>egr
F
G2
M
EdU
S
G1
G
DAPI
SA-β-gal
TRE-RFP
DAPI
SA-β-gal
rnts
H
rnts>egr
I
DAPI
E2F1-FUCCI
CycB-FUCCI
E2F1-FUCCI
CycB-FUCCI
rnts
J
rnts>egr

S1

843 **Figure S1. Cell cycle adaptations in response to inflammatory tissue damage**

844

845 **A.** Schematic illustrating the spatial organization of cell signaling and cell behavior in damaged tissue
846 following injury. The tissue repair region is divided into two spatially separated domains, indicated by
847 different colors. Senescent cells are located in the high JNK/AP1 signaling domain (magenta), while
848 regenerative proliferation occurs in the JAK/STAT signaling domain (cyan). See also (Cosolo et al, 2019;
849 Crucianelli et al, 2022; Floc'hlay et al, 2023; Jaiswal et al, 2023) for details.
850 **B, C.** Control wing disc (B) and a wing discs (C) after 24 hours of *egr*-expression within the wing pouch
851 domain under the control of the rn-GAL4 driver (rn^{ts} and rn^{ts}>egr, respectively). A co-expressed UAS-GFP
852 construct visualizes the rn-GAL4 expression domain. Staining for cleaved Dcp-1 visualizes apoptosis.
853 Discs were stained with DAPI to visualize nuclei. Please note the GFP-expression domain in (C) which
854 does not stain for cDcp-1 and represents surviving cells with high levels of JNK activity (see Fig 1B). Levels
855 of Dcp-1 were previously quantified (Cosolo et al, 2019; Jaiswal et al, 2023; La Fortezza et al, 2016).
856 **D-F.** Control (D) and *egr*-expressing wing disc (E), co-expressing the FUCCI cell cycle reporter system (F)
857 consisting of mRFP-NLS.CycB.1-266 (red in overlay) and GFP-E2f1.1-230 (green in overlay). Discs were
858 stained with DAPI to visualize nuclei. Cells in the Gap phase G1, express GFP; cells in early S-phase lack
859 expression of both FUCCI constructs; cells in late S-phase express RFP; and cells in G2 express both
860 reporters. Cell cycle changes were already previously quantified (Cosolo et al, 2019; Crucianelli et al,
861 2022; Jaiswal et al, 2023).
862 **G,H.** Analysis of senescence-associated β-galactosidase (SA-β-gal) activity (cyan or grey) in control (G)
863 and *egr*-expressing wing disc (H). TRE-RFP visualizes JNK-pathway activity. Discs were stained with DAPI
864 to visualize nuclei (magenta or grey). SA-β-gal activity was already previously reported and quantified
865 (Floc'hlay et al, 2023; Jaiswal et al, 2023).
866 **I,J.** Nota of control (I) and wing disc expressing egr in the pouch (J), co-expressing the FUCCI cell cycle
867 reporter system consisting of mRFP-NLS.CycB.1-266 (red in overlay) and GFP-E2f1.1-230 (green in
868 overlay) (as described in Fig-S1F). Discs were stained with DAPI to visualize nuclei.
869
870 Scale bars: 100 μm.
871
872

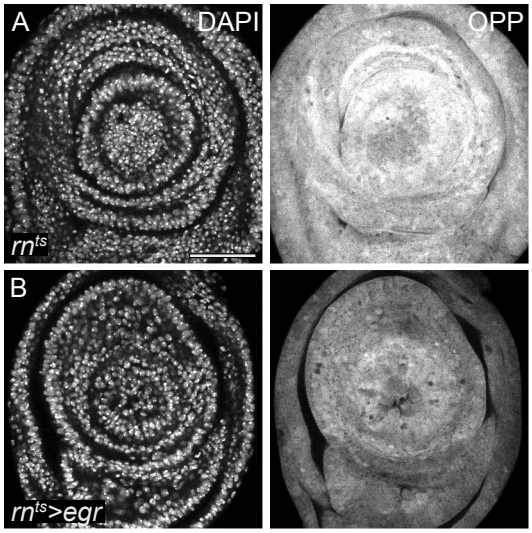

S2

873 **Figure S2. Metabolic adaptation in peripheral tissues**

874

875 **A, B.** Protein synthesis visualized by O-proparyl-puromycin (OPP) incorporation into newly synthesized
876 proteins in leg imaginal discs, dissected from larvae containing either control wing disc (A) or *egr*-
877 expressing wing discs (B). Discs were stained with DAPI to visualize nuclei.

878

879 Scale bar: 100 μm.

880

881

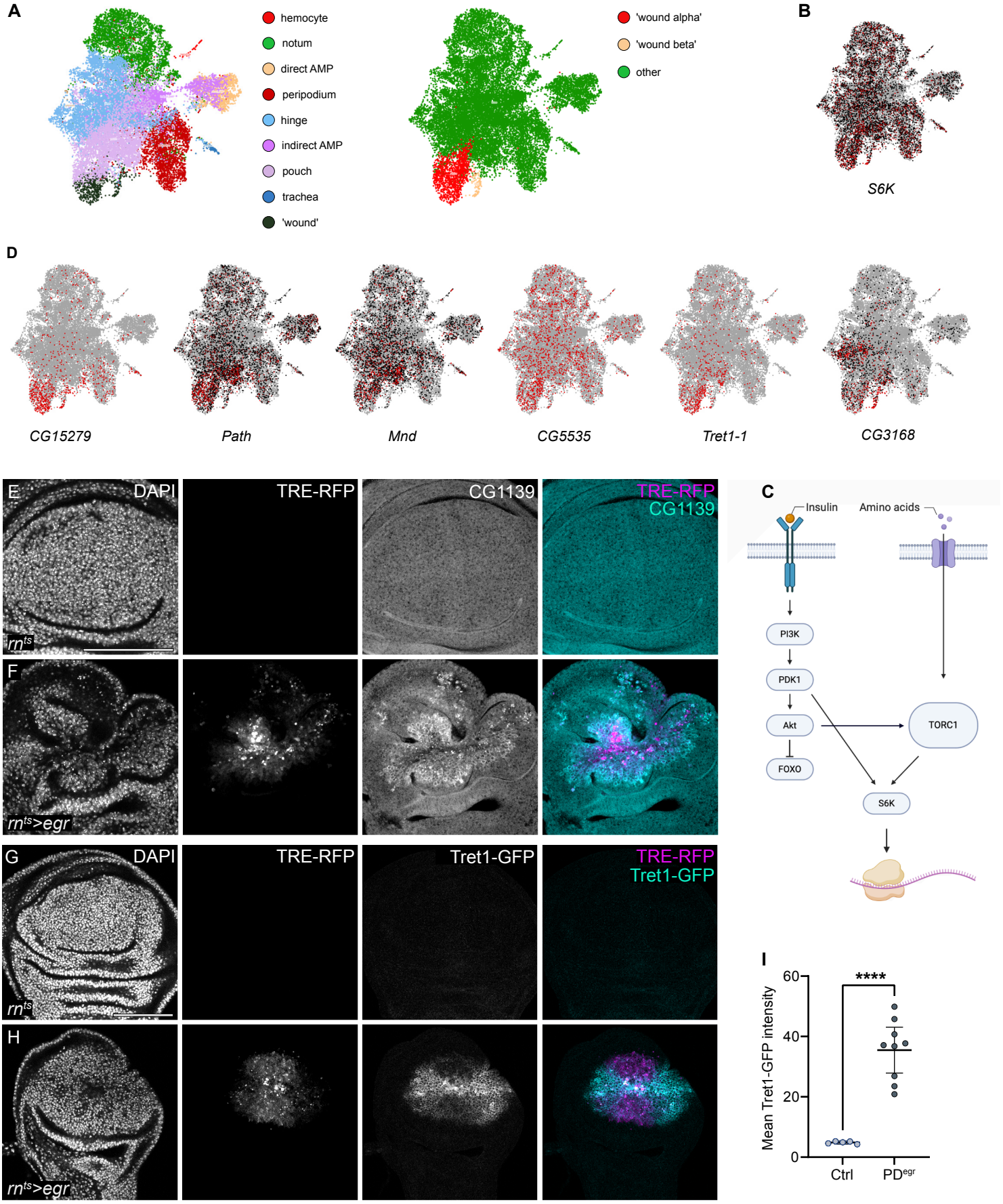
A
hemocyte
notum
direct AMP
peripodium
hinge
indirect AMP
pouch
trachea
'wound'
'wound alpha'
'wound beta'
other
B
S6K
D
CG15279
Path
Mnd
CG5535
Tret1-1
CG3168
E
DAPI
TRE-RFP
CG1139
TRE-RFP
CG1139
rn^ts
F
rn^ts>egr
G
DAPI
TRE-RFP
Tret1-GFP
TRE-RFP
Tret1-GFP
rn^ts
H
rn^ts>egr
C
Insulin
Amino acids
PI3K
PDK1
Akt
FOXO
TORC1
S6K
I
Mean Tret1-GFP intensity
60
40
20
0
****
Ctrl
PD^egr

S3

882 **Figure S3. Elevated levels of nutrient transporters and mTORC signaling support regenerative**
883 **proliferation**

884

885 **A.** UMAP plots generated using the Scope Wing Atlas created from control and *egr*-expressing discs
886 analysed by single-cell RNA-Seq technology (Floc'hlay et al, 2022). Left: A 'wound' cluster appears in *egr*-
887 expressing discs. Right: Further analysis revealed the identity of an alpha and beta cluster within *egr*-
888 expressing discs with signatures characteristic of senescent cells (beta) and with characteristic of a cell
889 and tissue damage response signature (alpha).
890 **B.** The scRNA UMAP plot displays the transcript levels of ribosomal protein S6 kinase (S6K). Grey indicates
891 low expression, and red indicates high expression of transcripts.
892 **C.** A scheme illustrating InR/PI3K/AKT and mTORC signaling pathways involved in growth and protein
893 synthesis in normal tissues.
894 **D.** scRNA UMAP plot displaying significantly elevated transcript levels detected for different nutrient
895 transporters in alpha and beta clusters (Floc'hlay et al, 2023). Grey indicates low expression, and red
896 indicates high expression of transcripts.
897 **E,F.** Staining for the putative alanine, glycine and proline amino acid transporter Arcus (CG1139, cyan or
898 grey) in control (E) and *egr*-expressing discs (F). TRE-RFP visualizes JNK-pathway activation (magenta or
899 grey). Discs were stained with DAPI to visualize nuclei.
900 **G,H.** Expression of Tret1.1-GFP (cyan or grey) in control (G) and *egr*-expressing discs (H). TRE-RFP
901 visualizes JNK-pathway activation (magenta or grey). Discs were stained with DAPI to visualize nuclei.
902 **I.** Mean Tret1.1-GFP intensity quantified in the pouch of control discs and the proliferative domain of *egr*-
903 expressing discs. Mean and 95% CI are shown. Statistical significance was tested using the Welch's t-
904 test, p-value < 0.0001 (control: n=5, *egr*-expressing discs: n=9).
905 Scale bar: 100 μm. Fluorescence intensities are reported as arbitrary units.
906
907
908

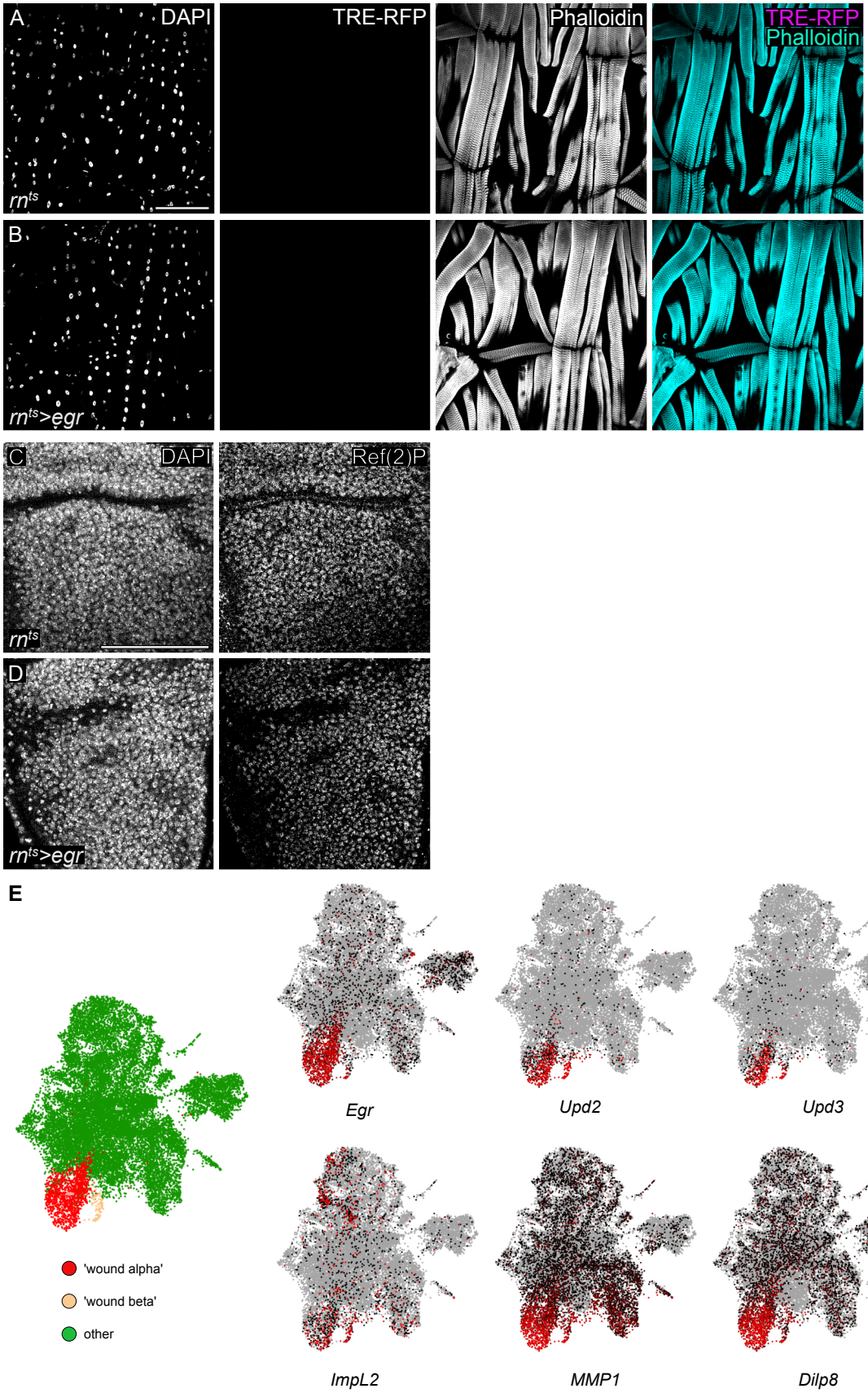
A
DAPI
TRE-RFP
Phalloidin
TRE-RFP
Phalloidin
rn^ts
B
rn^ts>egr
C
DAPI
Ref(2)P
rn^ts
D
rn^ts>egr
E
'wound alpha'
'wound beta'
other
Egr
Upd2
Upd3
ImpL2
MMP1
Dilp8

S4

Figure S4. Interorgan signals are induced by *egr*-driven inflammatory damage

---

A, B. *Drosophila* larval body wall muscles dissected from larvae containing either control (A) or *egr*-expressing (B) wing discs. Actin was visualized using Phalloidin (cyan or grey) and TRE-RFP visualizes JNK-pathway activation (magenta or grey). Muscles were stained with DAPI to visualize nuclei. Please note that muscles do not activate JNK-signaling in response to inflammatory cues.

C,D. Nota of control (C) and *egr*-expressing wing disc (D) stained for the autophagy marker Ref(2)P. Discs were stained with DAPI to visualize nuclei.

E. UMAP plots generated using the Scope Wing Atlas created from control and *egr*-expressing discs analysed by single-cell RNA-Seq technology (Floc'hlay et al, 2022). Significantly elevated transcript levels detected for different secreted paracrine ligands with known interorgan signaling roles in alpha and beta clusters are shown. Grey indicates low expression, and red indicates high expression of transcripts.

Scale bar: 100 μm.

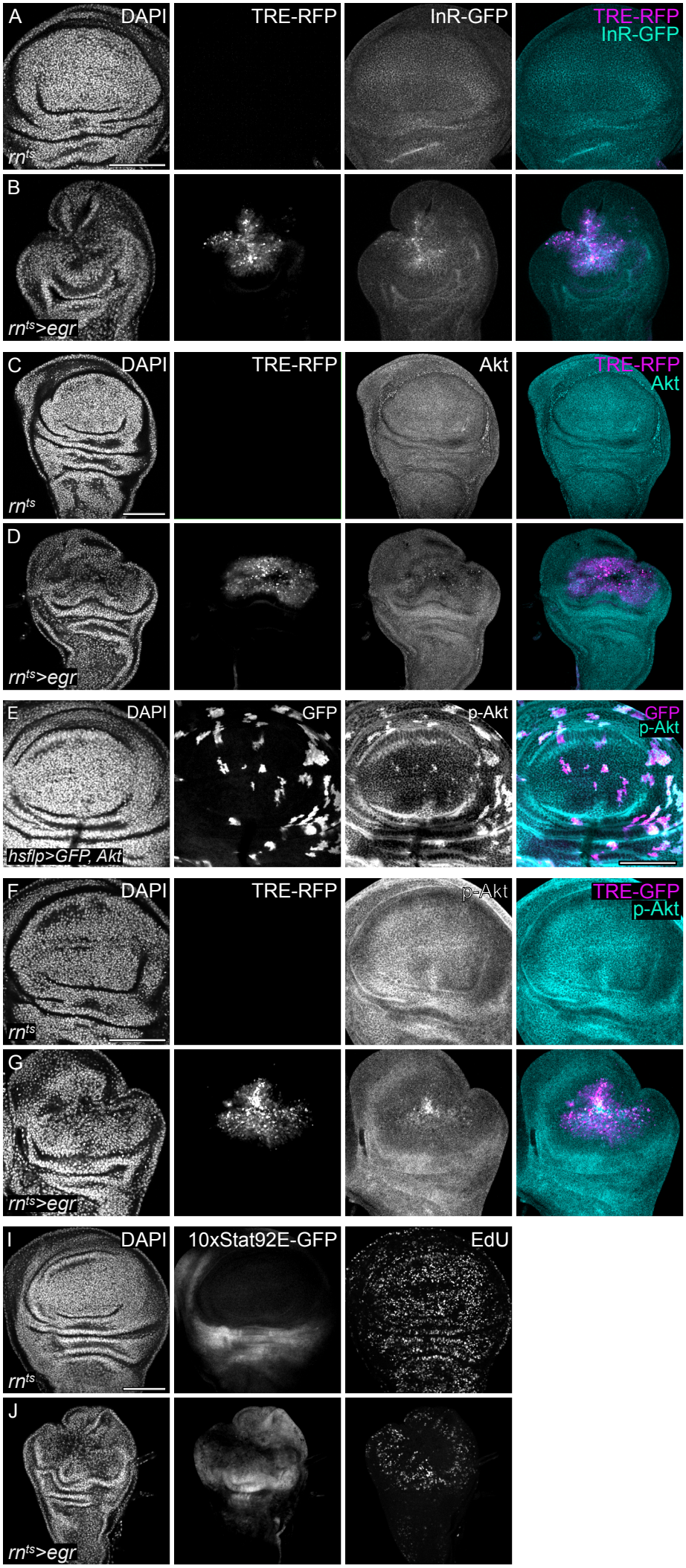
A
DAPI
TRE-RFP
InR-GFP
TRE-RFP
InR-GFP
rn^ts
B
rn^ts>egr
C
DAPI
TRE-RFP
Akt
TRE-RFP
Akt
rn^ts
D
rn^ts>egr
E
DAPI
GFP
p-Akt
GFP
p-Akt
hsflp>GFP, Akt
F
DAPI
TRE-RFP
p-Akt
TRE-GFP
p-Akt
rn^ts
G
rn^ts>egr
I
DAPI
10xStat92E-GFP
EdU
rn^ts
J
rn^ts>egr

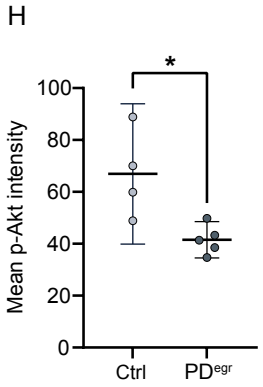
H
*
Mean p-Akt intensity
100
80
60
40
20
0
Ctrl
PD^egr

S5

925 **Figure S5. Insulin/PI3K/Akt signaling is low in the proliferative domain**

926

927 **A-D.** Control (A, C) and *egr*-expressing wing discs (B, D), expressing an Insulin receptor tagged with GFP
928 (InR-GFP) (A, B) or stained for Akt (C, D) (cyan or grey). TRE-RFP visualizes JNK-pathway activity (magenta
929 or grey). Discs were stained with DAPI to visualize nuclei.
930 **E.** Anti-phospho-Akt (S505) staining (cyan or grey) to test antibody specificity in UAS-Akt-overexpressing
931 clones marked by co-expression of UAS-GFP (magenta or grey) in the wing imaginal disc. Discs were
932 stained with DAPI to visualize nuclei.
933 **F,G.** Control (F) and *egr*-expressing wing discs (G), stained for phospho-Akt (S505) (cyan or grey). TRE-RFP
934 visualizes JNK-pathway activity (magenta or grey). Discs were stained with DAPI to visualize nuclei.
935 **H.** Quantification of mean p-Akt intensity in the control pouch and proliferative domain of *egr*-expressing
936 wing discs. Mean and 95% CI are shown and statistical significance was tested using an Unpaired t-test ,
937 p-value =0.0156. (Control; n=4, *egr*-expressing discs; n=5)
938 **I, J.** Control and *egr*-expressing discs stained for EdU to visualize DNA replication in discs also co-
939 expressing a 10xStat92E-GFP activity reporter (same disc is shown in Fig-1A). Discs were also stained
940 with DAPI to visualize nuclei. EdU intensity in 10xStat92E-GFP reporter-expressing domain was previously
941 quantified (Jaiswal et al, 2023).

942

943 Scale bar: 100 μm. Fluorescence intensities are reported as arbitrary units.

944

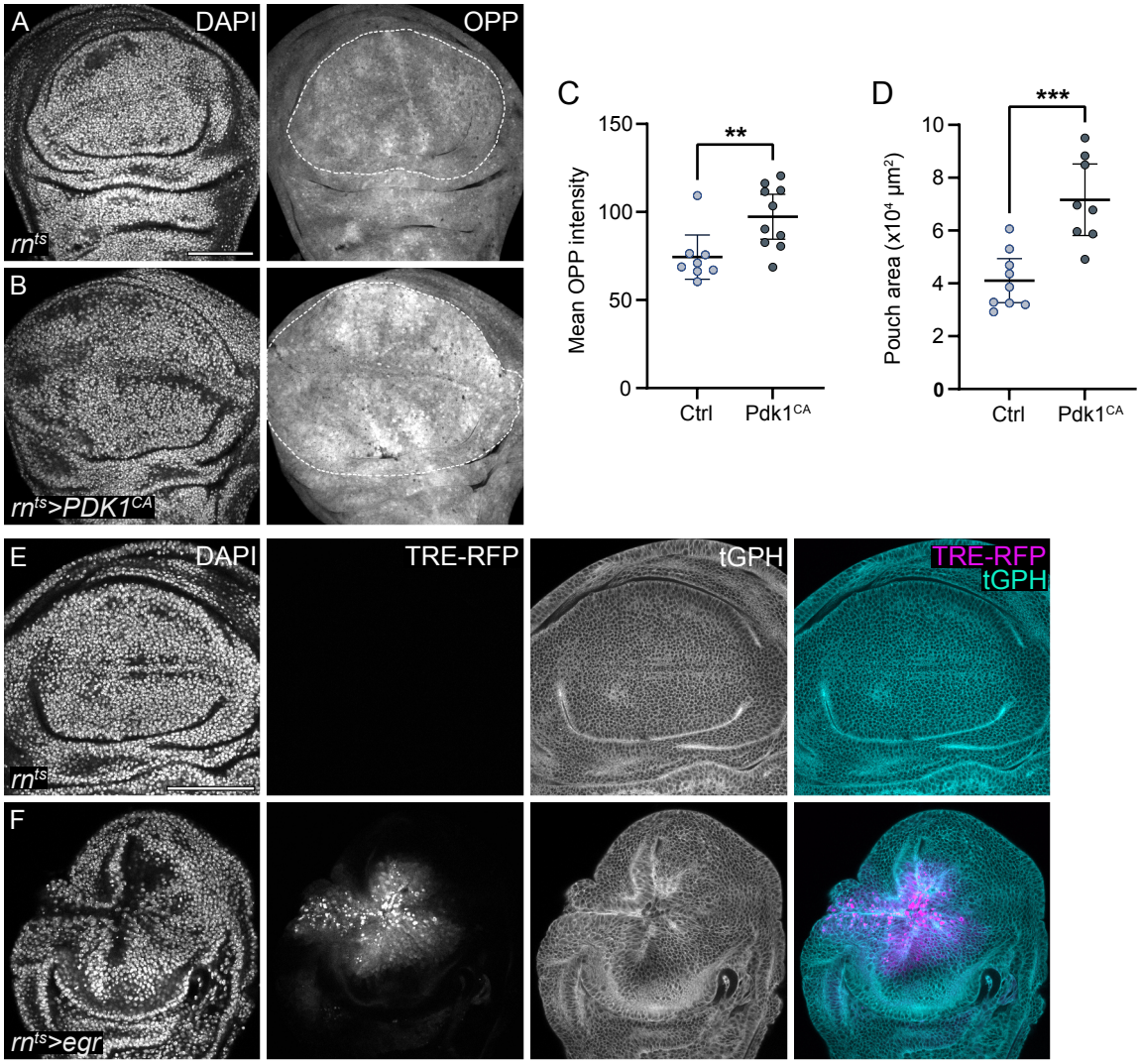
A
DAPI
OPP
rn^ts
B
rn^ts>PDK1^CA
C
Mean OPP intensity
150
100
50
0
**
Ctrl
Pdk1^CA
D
Pouch area (x10^4 µm^2)
10
8
6
4
2
0
***
Ctrl
Pdk1^CA
E
DAPI
TRE-RFP
tGPH
TRE-RFP
tGPH
rn^ts
F
rn^ts>egr

S6

945 **Figures S6. Pdk1 is sufficient to drive elevated protein synthesis in wing imaginal disc**

946

947 **A,B.** Protein synthesis visualized by OPP incorporation in control (A) and discs expressing a constitutively
948 active UAS-PDK1 (B) for 24 h under the control of rn-GAL4. Discs were stained with DAPI to visualize
949 nuclei. The dotted white line marks the border of the pouch using tissue fold landmarks.
950 **C.** Quantification of mean OPP intensity in the pouch of control and *Pdk1*^{CA}-expressing wing discs. Mean
951 and 95% CI are shown and statistical significance was tested using Mann-Whitney test. p-value = 0.0062.
952 (Control; n=8, *Pdk1*^{CA}-expressing discs; n=10).
953 **D.** Quantification of the pouch area in control and *Pdk1*^{CA}-expressing wing discs. Mean and 95% CI are
954 shown and statistical significance was tested using Unpaired t-test. p-value = 0.0003. (Control; n=9,
955 *Pdk1*^{CA}-expressing discs; n=8).
956 **E,F.** Control (E) and *egr*-expressing wing disc (F), also co-expressing the Pleckstrin Homology Domain
957 reporter for PIP3 levels (tGPH) (cyan or grey). TRE-RFP visualizes JNK-pathway activity (magenta or grey).
958 Discs were stained with DAPI to visualize nuclei.

959

960 Scale bar: 100 μm. Fluorescence intensities are reported as arbitrary units.

961

962 **Table S1 Drosophila strains**

963

Genotype	Source
Dilp8-GFP	BDSC: 33079
ImpL2-GFP	BDSC: 59778
UAS-ImpL2-3xHA	Fly-ORF F001712
Upd3.1-3 LacZ	Ishwar Hariharan lab
dFOXO-GFP	BDSC: 59766
en2.4-GAL4, UAS-mRPF.NLS/CyO	BDSC: 30557
Tret1-GFP	BDSC: 66367
Pdk1-GFP	BDSC: 59836
InR-eGFP	Hong Xu lab DOI: 10.7554/eLife.49309
tGPH-GFP	Yohanns Bellaiche
UAS-Akt1	BDSC: 8192
CG5535-GFP	BDSC: 64096
CycB-FUCCI': Ubi-mRFP1.NLS.CycB$^{1–266}$	Norman Zielke PMID: 24726363
E2F1-FUCCI, CycB-FUCCI'; Ubi-GFP.E2f1$^{1-230}$, Ubi-mRFP1.NLS.CycB$^{1-266}$	Norman Zielke PMID: 24726363
UAS-GFP^{S56T}	BDSC: 1521
rn$^{GAL4-DeltaS}$, tubGAL80^{ts}	BDSC: 8142, 7012
rn^{GAL4-5}, UAS-egr, tubP-GAL80^{ts}	Iswar Hariharan
10xStat92E-dGFP	Erica Bach PMID: 17008134
10xStat92E-GFP	Erica Bach PMID: 17008134
UAS-Stat92E.ORF.3xHA	Fly-ORF F000750 PMID: 23583758
'TRE-RFP': TRE-DsRed.T4	Dirk Bohmann PMID: 22509270
upd3.1-3-LacZ	Iswar Hariharan
UAS-dPdk1	Hugo Stocker
UAS-dPdk1(A467V)	Hugo Stocker https://doi.org/10.1073/pnas.011318098
dPdk1(5)ΔEP	Hugo Stocker lab https://doi.org/10.1073/pnas.011318098

964 **Table S2 Immunohistochemistry reagents**

965

Reagent	Source	
Mouse polyclonal anti-β-Galactosidase (1:1000)	Promega	Cat. #: Z3782
Mouse monoclonal anti-MMP-1 (1:30)	Developmental Studies Hybridoma Bank	Cat. #: 3A6B4
Mouse monoclonal anti-MMP-1 (1:30)	Developmental Studies Hybridoma Bank	Cat. #: 3B8D12
Mouse monoclonal anti-MMP-1 (1:30)	Developmental Studies Hybridoma Bank	Cat. #: 5H7B11
Mouse monoclonal anti-Nubbin (1:100)	Developmental Studies Hybridoma Bank	Cat. #: 2D4
Rabbit polyclonal anti-CG1139 (1:200)	Susumu Hirabayashi, Imperial College London Faculty of Medicine.	https://pubmed.ncbi.nlm.nih.gov/32938923/
Rabbit polyclonal anti-p-AKT (S505) (1:500)	Cell Signaling	Cat. #: 4084s
Rabbit polyclonal anti-AKT (1:500)	Cell Signaling	Cat. #: 9272s
Rat monoclonal anti-RFP (1:1000)	Chromotek	Cat. #: 5F8
Rabbit polyclonal anti-Drosophila p-S6 (1:200)	Aurelio Telemann, DKFZ	https://doi.org/10.1016/j.devcel.2017.07.019
Rabbit polyclonal anti-Ref(2)p	Abcam	Cat. #: Ab178440
Rabbit anti-cleaved Dcp-1	Cell Signaling	Cat. #: 9578s
Rabbit monoclonal anti-GFP	Invitrogen	Cat. #: G10362
Goat anti-mouse IgG Alexa Flour 488	Invitrogen	Cat. #: A-11001
Goat anti-rabbit IgG Alexa Flour 488	Invitrogen	Cat. #: A-11008
Goat anti-mouse IgG Alexa Flour 555	Invitrogen	Cat. #: A-21422
Goat anti-rat IgG Alexa Flour 555	Invitrogen	Cat. #: A-21434
Goat anti-mouse Alexa Flour 647	Invitrogen	Cat. #: A-21235
Goat anti-rabbit Alexa Flour 647	Invitrogen	Cat. #: A-21244
Click-iT Plus EdU Alexa Fluor 647 Imaging Kit	Invitrogen	Cat. #: C10340
Phalloidin 488	Invitrogen	Cat #: A12379
Phalloidin 647	Invitrogen	Cat #: A22287
DAPI	Sigma Aldrich	Cat #: D9564
CellEvent Senescence Green Detection Kit	Invitrogen	Cat. #: C10850

Rapamycin	Thermo Fisher Scientific	Cat. #: J62473.MC
Click-iT Plus OPP Alexa Fluor 647 Imaging Kit	Invitrogen	Cat. #: C10458
Leptomycin	Sigma-Aldrich	Cat. #: L2913
Nile Red	Invitrogen	Cat. #: N1142

968 **References**

969

970 Agrawal, N., Delanoue, R., Mauri, A., Basco, D., Pasco, M., Thorens, B. & Leopold, P. (2016) The Drosophila TNF
971 Eiger Is an Adipokine that Acts on Insulin-Producing Cells to Mediate Nutrient Response. *Cell Metab*, 23(4), 675-
972 84.

973 Albina, J. E., Abate, J. A. & Mastrofrancesco, B. (1993) Role of ornithine as a proline precursor in healing wounds.
974 *J Surg Res*, 55(1), 97-102.

975 Altman, B. J., Stine, Z. E. & Dang, C. V. (2016) From Krebs to clinic: glutamine metabolism to cancer therapy.
976 *Nat Rev Cancer*, 16(10), 619-34.

977 Argiles, J. M., Busquets, S., Stemmler, B. & Lopez-Soriano, F. J. (2014) Cancer cachexia: understanding the
978 molecular basis. *Nat Rev Cancer*, 14(11), 754-62.

979 Aviner, R. (2020) The science of puromycin: From studies of ribosome function to applications in biotechnology.
980 *Comput Struct Biotechnol J*, 18, 1074-1083.

981 Bilder, D., Ong, K., Hsi, T. C., Adiga, K. & Kim, J. (2021) Tumour-host interactions through the lens of Drosophila.
982 *Nat Rev Cancer*, 21(11), 687-700.

983 Boulan, L., Andersen, D., Colombani, J., Boone, E. & Leopold, P. (2019) Inter-Organ Growth Coordination Is
984 Mediated by the Xrp1-Dilp8 Axis in Drosophila. *Dev Cell*, 49(5), 811-818 e4.

985 Britton, J. S., Lockwood, W. K., Li, L., Cohen, S. M. & Edgar, B. A. (2002) Drosophila's insulin/PI3-kinase pathway
986 coordinates cellular metabolism with nutritional conditions. *Dev Cell*, 2(2), 239-49.

987 Cao, X., Rojas, M. & Pastor-Pareja, J. C. (2022) Intrinsic and damage-induced JAK/STAT signaling regulate
988 developmental timing by the Drosophila prothoracic gland. *Dis Model Mech*, 15(1).

989 Chatterjee, N. & Bohmann, D. (2012) A versatile PhiC31 based reporter system for measuring AP-1 and Nrf2
990 signaling in Drosophila and in tissue culture. *PLoS One*, 7(4), e34063.

991 Colombani, J., Andersen, D. S. & Leopold, P. (2012) Secreted peptide Dilp8 coordinates Drosophila tissue growth
992 with developmental timing. *Science*, 336(6081), 582-5.

993 Cong, B., Nakamura, M., Sando, Y., Kondo, T., Ohsawa, S. & Igaki, T. (2021) JNK and Yorkie drive tumor
994 malignancy by inducing L-amino acid transporter 1 in Drosophila. *PLoS Genet*, 17(11), e1009893.

995 Cosolo, A., Jaiswal, J., Csordas, G., Grass, I., Uhlirova, M. & Classen, A. K. (2019) JNK-dependent cell cycle stalling
996 in G2 promotes survival and senescence-like phenotypes in tissue stress. *Elife*, 8.

997 Crucianelli, C., Jaiswal, J., Vijayakumar Maya, A., Nogay, L., Cosolo, A., Grass, I. & Classen, A. K. (2022) Distinct
998 signaling signatures drive compensatory proliferation via S-phase acceleration. *PLoS Genet*, 18(12), e1010516.

999 Destefanis, F., Manara, V. & Bellosta, P. (2020) Myc as a Regulator of Ribosome Biogenesis and Cell
1000 Competition: A Link to Cancer. *Int J Mol Sci*, 21(11).

1001 Ding, G., Xiang, X., Hu, Y., Xiao, G., Chen, Y., Binari, R., Comjean, A., Li, J., Rushworth, E., Fu, Z., Mohr, S. E.,
1002 Perrimon, N. & Song, W. (2021) Coordination of tumor growth and host wasting by tumor-derived Upd3. *Cell*
1003 *Rep*, 36(7), 109553.

1004 Dvorak, H. F. (1986) Tumors: wounds that do not heal. Similarities between tumor stroma generation and
1005 wound healing. *N Engl J Med*, 315(26), 1650-9.

1006 Edwards-Hicks, J., Mitterer, M., Pearce, E. L. & Buescher, J. M. (2020) Metabolic Dynamics of In Vitro CD8+ T
1007 Cell Activation. *Metabolites*, 11(1).

1008 Eming, S. A., Murray, P. J. & Pearce, E. J. (2021) Metabolic orchestration of the wound healing response. *Cell*
1009 *Metab*, 33(9), 1726-1743.

1010 Eming, S. A., Wynn, T. A. & Martin, P. (2017) Inflammation and metabolism in tissue repair and regeneration.
1011 *Science*, 356(6342), 1026-1030.

1012 Enomoto, M. & Igaki, T. (2022) Cell-cell interactions that drive tumorigenesis in Drosophila. *Fly (Austin)*, 16(1),
1013 367-381.

1014 Figueroa-Clarevega, A. & Bilder, D. (2015) Malignant Drosophila tumors interrupt insulin signaling to induce
1015 cachexia-like wasting. *Dev Cell*, 33(1), 47-55.

1016 Floc'hlay, S., Balaji, R., Christiaens, V., González-Blas, C. B., De Winter, S., Hulselmans, G., De Waegeneer, M.,
1017 Quan, X., Koldere, D., Atkins, M., Halder, G., Classen, A.-K. & Aerts, S. (2022) Shared enhancer gene regulatory
1018 networks between wound and oncogenic programs. *Biorxiv*.

1019 Floc'hlay, S., Balaji, R., Stankovic, D., Christiaens, V. M., Bravo Gonzalez-Blas, C., De Winter, S., Hulselmans, G.
1020 J., De Waegeneer, M., Quan, X., Koldere, D., Atkins, M., Halder, G., Uhlirova, M., Classen, A. K. & Aerts, S. (2023)
1021 Shared enhancer gene regulatory networks between wound and oncogenic programs. *Elife*, 12.

1022 Fox, D. T., Cohen, E. & Smith-Bolton, R. (2020) Model systems for regeneration: Drosophila. *Development*,
1023 147(7).

1024 Garelli, A., Gontijo, A. M., Miguela, V., Caparros, E. & Dominguez, M. (2012) Imaginal discs secrete insulin-like
1025 peptide 8 to mediate plasticity of growth and maturation. *Science*, 336(6081), 579-82.

1026 Gontijo, A. M. & Garelli, A. (2018) The biology and evolution of the Dilp8-Lgr3 pathway: A relaxin-like pathway
1027 coupling tissue growth and developmental timing control. *Mechanisms of Development.* Elsevier Ireland Ltd.

1028 Hackney, J. F. & Cherbas, P. (2014) Injury response checkpoint and developmental timing in insects. *Fly (Austin)*,
1029 8(4), 226-31.

1030 Halme, A., Cheng, M. & Hariharan, I. K. (2010) Retinoids regulate a developmental checkpoint for tissue
1031 regeneration in Drosophila. *Curr Biol*, 20(5), 458-63.

1032 Herrera, S. C. & Bach, E. A. (2019) JAK/STAT signaling in stem cells and regeneration: from Drosophila to
1033 vertebrates. *Development*, 146(2).

1034 Herrera, S. C., Martin, R. & Morata, G. (2013) Tissue homeostasis in the wing disc of Drosophila melanogaster:
1035 immediate response to massive damage during development. *PLoS Genet*, 9(4), e1003446.

1036 Hodgson, J. A., Parvy, J. P., Yu, Y., Vidal, M. & Cordero, J. B. (2021) Drosophila Larval Models of Invasive
1037 Tumorigenesis for In Vivo Studies on Tumour/Peripheral Host Tissue Interactions during Cancer Cachexia. *Int J*
1038 *Mol Sci*, 22(15).

1039 Holz, M. K., Ballif, B. A., Gygi, S. P. & Blenis, J. (2005) mTOR and S6K1 mediate assembly of the translation
1040 preinitiation complex through dynamic protein interchange and ordered phosphorylation events. *Cell*, 123(4),
1041 569-80.

1042 Hopkins, B. D., Goncalves, M. D. & Cantley, L. C. (2020) Insulin-PI3K signalling: an evolutionarily insulated
1043 metabolic driver of cancer. *Nat Rev Endocrinol*, 16(5), 276-283.

1044 Hoxhaj, G. & Manning, B. D. (2020) The PI3K-AKT network at the interface of oncogenic signalling and cancer
1045 metabolism. *Nat Rev Cancer*, 20(2), 74-88.

1046 Huang, W., Hickson, L. J., Eirin, A., Kirkland, J. L. & Lerman, L. O. (2022) Cellular senescence: the good, the bad
1047 and the unknown. *Nat Rev Nephrol*, 18(10), 611-627.

1048 Ingaramo, M. C., Sanchez, J. A., Perrimon, N. & Dekanty, A. (2020) Fat Body p53 Regulates Systemic Insulin
1049 Signaling and Autophagy under Nutrient Stress via Drosophila Upd2 Repression. *Cell Rep*, 33(4), 108321.

1050 Jaiswal, J., Egert, J., Engesser, R., Peyroton, A. A., Nogay, L., Weichselberger, V., Crucianelli, C., Grass, I., Kreutz,
1051 C., Timmer, J. & Classen, A. K. (2023) Mutual repression between JNK/AP-1 and JAK/STAT stratifies senescent
1052 and proliferative cell behaviors during tissue regeneration. *PLoS Biol*, 21(5), e3001665.

1053 Jewell, J. L., Russell, R. C. & Guan, K. L. (2013) Amino acid signalling upstream of mTOR. *Nat Rev Mol Cell Biol*,
1054 14(3), 133-9.

1055 Jiang, H., Kimura, T., Hai, H., Yamamura, R. & Sonoshita, M. (2022) Drosophila as a toolkit to tackle cancer and
1056 its metabolism. *Front Oncol*, 12, 982751.

1057 Kakanj, P., Moussian, B., Gronke, S., Bustos, V., Eming, S. A., Partridge, L. & Leptin, M. (2016) Insulin and TOR
1058 signal in parallel through FOXO and S6K to promote epithelial wound healing. *Nat Commun*, 7, 12972.

1059 Kashio, S. & Miura, M. (2020) Kynurenine Metabolism in the Fat Body Non-autonomously Regulates Imaginal
1060 Disc Repair in Drosophila. *iScience*, 23(12), 101738.

1061 Kashio, S., Obata, F., Zhang, L., Katsuyama, T., Chihara, T. & Miura, M. (2016) Tissue nonautonomous effects of
1062 fat body methionine metabolism on imaginal disc repair in Drosophila. *Proc Natl Acad Sci U S A*, 113(7), 1835-
1063 40.

1064 Katheder, N. S. & Rusten, T. E. (2017) Microenvironment and tumors-a nurturing relationship. *Autophagy*,
1065 13(7), 1241-1243.

1066 Keshet, R., Szlosarek, P., Carracedo, A. & Erez, A. (2018) Rewiring urea cycle metabolism in cancer to support
1067 anabolism. *Nat Rev Cancer*, 18(10), 634-645.

1068 Khezri, R., Holland, P., Schoborg, T. A., Abramovich, I., Takats, S., Dillard, C., Jain, A., O'Farrell, F., Schultz, S. W.,
1069 Hagopian, W. M., Quintana, E. M., Ng, R., Katheder, N. S., Rahman, M. M., Teles Reis, J. G., Brech, A., Jasper, H.,
1070 Rusan, N. M., Jahren, A. H., Gottlieb, E. & Rusten, T. E. (2021) Host autophagy mediates organ wasting and
1071 nutrient mobilization for tumor growth. *EMBO J*, 40(18), e107336.

1072 Kwon, Y., Song, W., Droujinine, I. A., Hu, Y., Asara, J. M. & Perrimon, N. (2015) Systemic organ wasting induced
1073 by localized expression of the secreted insulin/IGF antagonist ImpL2. *Dev Cell*, 33(1), 36-46.

1074 La Fortezza, M., Schenk, M., Cosolo, A., Kolybaba, A., Grass, I. & Classen, A. K. (2016) JAK/STAT signalling
1075 mediates cell survival in response to tissue stress. *Development*, 143(16), 2907-19.

1076 La Marca, J. E. & Richardson, H. E. (2020) Two-Faced: Roles of JNK Signalling During Tumourigenesis in the
1077 Drosophila Model. *Front Cell Dev Biol*, 8, 42.

1078 Lama-Sherpa, T. D., Jeong, M. H. & Jewell, J. L. (2023) Regulation of mTORC1 by the Rag GTPases. *Biochem Soc*
1079 *Trans*, 51(2), 655-664.

1080 Lee, J., Ng, K. G., Dombek, K. M., Eom, D. S. & Kwon, Y. V. (2021) Tumors overcome the action of the wasting
1081 factor ImpL2 by locally elevating Wnt/Wingless. *Proc Natl Acad Sci U S A*, 118(23).

1082 Levina, A., Fleming, K. D., Burke, J. E. & Leonard, T. A. (2022) Activation of the essential kinase PDK1 by
1083 phosphoinositide-driven trans-autophosphorylation. *Nat Commun*, 13(1), 1874.

1084 Li, J., Kim, S. G. & Blenis, J. (2014) Rapamycin: One drug, many effects. *Cell Metabolism.*

1085 Lieu, E. L., Nguyen, T., Rhyne, S. & Kim, J. (2020) Amino acids in cancer. *Exp Mol Med*, 52(1), 15-30.

1086 Ling, Z. N., Jiang, Y. F., Ru, J. N., Lu, J. H., Ding, B. & Wu, J. (2023) Amino acid metabolism in health and disease.
1087 *Signal Transduct Target Ther*, 8(1), 345.

1088 Liu, G. Y. & Sabatini, D. M. (2020) mTOR at the nexus of nutrition, growth, ageing and disease. *Nat Rev Mol Cell*
1089 *Biol*, 21(4), 183-203.

1090 Liu, Y., Saavedra, P. & Perrimon, N. (2022) Cancer cachexia: lessons from Drosophila. *Dis Model Mech*, 15(3).

1091 Lodge, W., Zavortink, M., Golenkina, S., Froldi, F., Dark, C., Cheung, S., Parker, B. L., Blazev, R., Bakopoulos, D.,
1092 Christie, E. L., Wimmer, V. C., Duckworth, B. C., Richardson, H. E. & Cheng, L. Y. (2021) Tumor-derived MMPs
1093 regulate cachexia in a Drosophila cancer model. *Dev Cell*, 56(18), 2664-2680 e6.

1094 MacCarthy-Morrogh, L. & Martin, P. (2020) *W O U N D H E A L I N G The hallmarks of cancer are also the*
1095 *hallmarks of wound healing*.

1096 Manning, B. D. & Cantley, L. C. (2007) AKT/PKB signaling: navigating downstream. *Cell*, 129(7), 1261-74.

1097 Marti, I. L. A. A. & Reith, W. (2021) Arginine-dependent immune responses. *Cell Mol Life Sci*, 78(13), 5303-5324.

1098 Martinez-Reyes, I. & Chandel, N. S. (2021) Cancer metabolism: looking forward. *Nat Rev Cancer*, 21(10), 669-
1099 680.

1100 Meacham, C. E., DeVilbiss, A. W. & Morrison, S. J. (2022) Metabolic regulation of somatic stem cells in vivo. *Nat*
1101 *Rev Mol Cell Biol*, 23(6), 428-443.

1102 Nakamura, M., Verboon, J. M., Allen, T. E., Abreu-Blanco, M. T., Liu, R., Dominguez, A. N. M., Delrow, J. J. &
1103 Parkhurst, S. M. (2020) Autocrine insulin pathway signaling regulates actin dynamics in cell wound repair. *PLoS*
1104 *Genet*, 16(12), e1009186.

1105 Newton, H., Wang, Y. F., Camplese, L., Mokochinski, J. B., Kramer, H. B., Brown, A. E. X., Fets, L. & Hirabayashi,
1106 S. (2020) Systemic muscle wasting and coordinated tumour response drive tumourigenesis. *Nat Commun*,
1107 11(1), 4653.

1108 Pena, O. A. & Martin, P. (2024) Cellular and molecular mechanisms of skin wound healing. *Nat Rev Mol Cell*
1109 *Biol*.

1110 Radimerski, T., Montagne, J., Rintelen, F., Stocker, H., van der Kaay, J., Downes, C. P., Hafen, E. & Thomas, G.
1111 (2002) dS6K-regulated cell growth is dPKB/dPI(3)K-independent, but requires dPDK1. *Nat Cell Biol*, 4(3), 251-5.

1112 Rajan, A. & Perrimon, N. (2012) Drosophila cytokine unpaired 2 regulates physiological homeostasis by
1113 remotely controlling insulin secretion. *Cell*, 151(1), 123-37.

1114 Ring, N. A. R., Dworak, H., Bachmann, B., Schadl, B., Valdivieso, K., Rozmaric, T., Heimel, P., Fischer, I., Klinaki,
1115 E., Gutasi, A., Schuetzenberger, K., Leinfellner, G., Ferguson, J., Drechsler, S., Mildner, M., Schosserer, M.,
1116 Slezak, P., Meyuhas, O., Gruber, F., Grillari, J., Redl, H. & Ogrodnik, M. (2023) The p-rpS6-zone delineates
1117 wounding responses and the healing process. *Dev Cell*, 58(11), 981-992 e6.

1118 Rintelen, F., Stocker, H., Thomas, G. & Hafen, E. (2001) PDK1 regulates growth through Akt and S6K in
1119 Drosophila. *Proc Natl Acad Sci U S A*, 98(26), 15020-5.

1120 Romao, D., Muzzopappa, M., Barrio, L. & Milan, M. (2021) The Upd3 cytokine couples inflammation to
1121 maturation defects in Drosophila. *Curr Biol*, 31(8), 1780-1787 e6.

1122 Rybinski, B., Franco-Barraza, J. & Cukierman, E. (2014) The wound healing, chronic fibrosis, and cancer
1123 progression triad. *Physiol Genomics*, 46(7), 223-44.

1124 Santabarbara-Ruiz, P. & Leopold, P. (2021) An Oatp transporter-mediated steroid sink promotes tumor-induced
1125 cachexia in Drosophila. *Dev Cell*, 56(19), 2741-2751 e7.

1126 Santabarbara-Ruiz, P., Lopez-Santillan, M., Martinez-Rodriguez, I., Binagui-Casas, A., Perez, L., Milan, M.,
1127 Corominas, M. & Serras, F. (2015) ROS-Induced JNK and p38 Signaling Is Required for Unpaired Cytokine
1128 Activation during Drosophila Regeneration. *PLoS Genet*, 11(10), e1005595.

1129 Saxton, R. A. & Sabatini, D. M. (2017) mTOR Signaling in Growth, Metabolism, and Disease. *Cell*, 168(6), 960-
1130 976.

1131 Schindelin, J., Arganda-Carreras, I., Frise, E., Kaynig, V., Longair, M., Pietzsch, T., Preibisch, S., Rueden, C.,
1132 Saalfeld, S., Schmid, B., Tinevez, J. Y., White, D. J., Hartenstein, V., Eliceiri, K., Tomancak, P. & Cardona, A. (2012)
1133 Fiji: an open-source platform for biological-image analysis. *Nat Methods*, 9(7), 676-82.

1134 Setiawan, T., Sari, I. N., Wijaya, Y. T., Julianto, N. M., Muhammad, J. A., Lee, H., Chae, J. H. & Kwon, H. Y. (2023)
1135 Cancer cachexia: molecular mechanisms and treatment strategies. *J Hematol Oncol*, 16(1), 54.

1136 Shi, H. P., Fishel, R. S., Efron, D. T., Williams, J. Z., Fishel, M. H. & Barbul, A. (2002) Effect of supplemental
1137 ornithine on wound healing. *J Surg Res*, 106(2), 299-302.

1138 Shimobayashi, M. & Hall, M. N. (2016) Multiple amino acid sensing inputs to mTORC1. *Cell Research.* Nature
1139 Publishing Group.

1140 Smith-Bolton, R. K., Worley, M. I., Kanda, H. & Hariharan, I. K. (2009) Regenerative growth in Drosophila
1141 imaginal discs is regulated by Wingless and Myc. *Dev Cell*, 16(6), 797-809.

1142 Song, W., Kir, S., Hong, S., Hu, Y., Wang, X., Binari, R., Tang, H. W., Chung, V., Banks, A. S., Spiegelman, B. &
1143 Perrimon, N. (2019) Tumor-Derived Ligands Trigger Tumor Growth and Host Wasting via Differential MEK
1144 Activation. *Dev Cell*, 48(2), 277-286 e6.

1145 Stevens, L. J. & Page-McCaw, A. (2012) A secreted MMP is required for reepithelialization during wound
1146 healing. *Mol Biol Cell*, 23(6), 1068-79.

1147 Stine, Z. E., Schug, Z. T., Salvino, J. M. & Dang, C. V. (2022) Targeting cancer metabolism in the era of precision
1148 oncology. *Nat Rev Drug Discov*, 21(2), 141-162.

1149 Sun, F. & Poss, K. D. (2023) Inter-organ communication during tissue regeneration. *Development*, 150(23).

1150 Sustar, A., Bonvin, M., Schubiger, M. & Schubiger, G. (2011) Drosophila twin spot clones reveal cell division
1151 dynamics in regenerating imaginal discs. *Dev Biol*, 356(2), 576-87.

1152 Vallejo, D. M., Juarez-Carreno, S., Bolivar, J., Morante, J. & Dominguez, M. (2015) A brain circuit that
1153 synchronizes growth and maturation revealed through Dilp8 binding to Lgr3. *Science*, 350(6262), aac6767.

1154 Witte, M. B. & Barbul, A. (2003) Arginine physiology and its implication for wound healing. *Wound Repair*
1155 *Regen*, 11(6), 419-23.

1156 Wong, K. K. L. & Verheyen, E. M. (2021) Metabolic reprogramming in cancer: Mechanistic insights from
1157 Drosophila. *DMM Disease Models and Mechanisms.* Company of Biologists Ltd.

1158 Worley, M. I., Everetts, N. J., Yasutomi, R., Chang, R. J., Saretha, S., Yosef, N. & Hariharan, I. K. (2022) Ets21C
1159 sustains a pro-regenerative transcriptional program in blastema cells of Drosophila imaginal discs. *Curr Biol*,
1160 32(15), 3350-3364 e6.

1161 Worley, M. I. & Hariharan, I. K. (2022) Imaginal Disc Regeneration: Something Old, Something New. *Cold Spring*
1162 *Harb Perspect Biol*, 14(11).

1163 Wu, X., Xie, W., Xie, W., Wei, W. & Guo, J. (2022) Beyond controlling cell size: functional analyses of S6K in
1164 tumorigenesis. *Cell Death Dis*, 13(7), 646.

1165 Yue, S., Li, G., He, S. & Li, T. (2022) The Central Role of mTORC1 in Amino Acid Sensing. *Cancer Res*, 82(17),
1166 2964-2974.

1167 Zheng, N., Wei, J., Wu, D., Xu, Y. & Guo, J. (2023) Master kinase PDK1 in tumorigenesis. *Biochim Biophys Acta*
1168 *Rev Cancer*, 1878(6), 188971.

1169 Zhu, J. & Thompson, C. B. (2019) Metabolic regulation of cell growth and proliferation. *Nat Rev Mol Cell Biol*,
1170 20(7), 436-450.

1171 Zielke, N., Korzelius, J., van Straaten, M., Bender, K., Schuhknecht, G. F. P., Dutta, D., Xiang, J. & Edgar, B. A.
1172 (2014) Fly-FUCCI: A versatile tool for studying cell proliferation in complex tissues. *Cell Rep*, 7(2), 588-598.
1173

1174